Catalytic Activity Maps for Alloy Nanoparticles

Liang Cao[1,*], Tim Mueller[2,*]

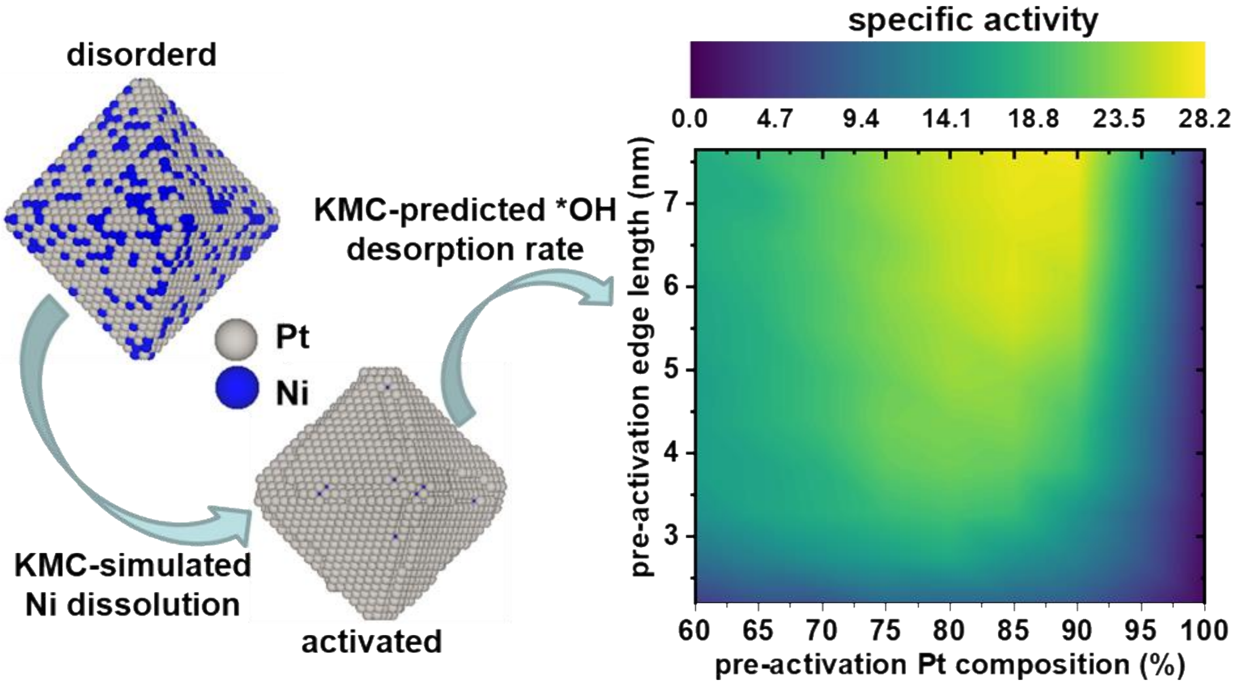

[1]Institute of Catalysis, Department of Chemistry, Zhejiang University, Hangzhou, Zhejiang 310058, P. R. China

[2]Department of Materials Science and Engineering, Johns Hopkins University, Baltimore, Maryland 21218, United States

Abstract

To enable rational design of alloy nanoparticle catalysts, we develop an approach to generate catalytic activity maps of alloy nanoparticles on a grid of particle size and composition. The catalytic activity maps are created by using a quaternary cluster expansion to explicitly predict adsorbate binding energies on alloy nanoparticles of varying shape, size, and atomic order while accounting for interactions among the adsorbates. This cluster expansion is used in kinetic Monte Carlo simulations to predict activated nanoparticle structures and turnover frequencies on all surface sites. We demonstrate our approach on Pt–Ni octahedral nanoparticle catalysts for the oxygen reduction reaction (ORR), revealing that the specific activity is predicted to be optimized at an edge length of larger than 5.5 nm and a composition of about $Pt_{0.85}Ni_{0.15}$ and the mass activity is predicted to be optimized at an edge length of 3.3 nm – 3.8 nm and a composition of about $Pt_{0.8}Ni_{0.2}$.

Keywords: rational design, intermetallic, solid-solution, cluster expansion, density functional theory, Pt–Ni catalysts, oxygen reduction reaction

Introduction

Alloy nanoparticles are well suited to be catalysts due to their high surface to volume ratios and the abundance of ways in which the structures and properties of the catalysts can be tailored. Various experimental synthesis strategies (e.g., core-shell[1], doping[2-4], shape-engineering[5]) have been used to improve the catalytic activity and stability of alloy nanocatalysts, but to limit the number of costly and time consuming experiments that must be done there is great interest in rational nanocatalyst design. Unfortunately, computational design of alloy nanocatalysts remains a significant challenge due to their size and complexity. Density functional theory (DFT)[6] calculations in standard implementations scale with the number of valence electrons as $O(N^3)$,[7] limiting the diameter of nanoparticles that can be practically modelled to about 2–3 nm, below the typical diameters (4–10 nm) of particles evaluated experimentally.[2, 4, 5, 8, 9] In addition, the arrangement of atoms in a substitutional alloy can dramatically affect its catalytic properties,[10, 11] making the computational prediction of the atomic structure of the catalyst a critically important step in the design process. Predicting the structure of a substitutional nanoalloy either through thermodynamic[2, 12-14] or kinetic[3, 15, 16] modelling requires the evaluation of the energies of a large number of candidate structures, where the energy differences between competing alloy structures can be on the order of meV / atom.[17] The design of alloy nanocatalysts is further complicated by the need to accurately predict adsorbate binding energies, an important descriptor of catalytic activity, on a variety of possible adsorption sites.

Various approaches have been used to computationally predict the structures and properties of alloy nanocatalysts. One strategy is to study nanoparticles that are small enough (~2 nm in diameter) to be modeled using DFT.[2, 18-20] However the cost of DFT calculations limits the number of structures that can be evaluated this way, and this approach cannot in practice be used to model particles of typical experimental sizes. Alternatively, nanoparticle facets may be approximated as extended surfaces, on which adsorbate binding energies can be calculated using DFT.[3, 11, 21, 22] The disadvantage of this approach is that it does not fully account for the variety of binding sites, including sites near edges and vertices, on a nanoparticle surface.

Due to the cost of directly using DFT, there has recently been significant interest in developing fast and accurate surrogate models for nanocatalysts. Calle-Vallejo et al.[23, 24] developed an approach in which the *OH and *OOH adsorption energies on Pt nanoparticles were linearly correlated with the generalized coordination number (GCN) of the surface binding site, which takes both the first- and second-nearest neighbors into account. The GCN model has inspired the rational design of highly active monometallic nanoparticles with varied shapes[25-28] and has also been used to model the strain effect by introducing the interatomic distance difference between surface and bulk metal atoms.[29] Jinnouchi et al.[30] developed a machine-learned interatomic potential model based on the smooth overlap of atomic positions (SOAP) kernel[31] to predict structures, catalytic activities, and N, O, and NO adsorption energies for fixed-shape Au–Rh nanoparticles with varied sizes. For catalysts with structures that can be mapped to a lattice model (e.g., an fcc lattice), formation energies can be accurately calculated using cluster expansions.[2, 3, 13, 19, 20, 32] This approach can be extended to the calculation of adsorption energies by including coordination-number-dependent and metal-specific correction terms into DFT-parametrized cluster expansions[3, 15], or by explicitly including adsorbates in the cluster expansion as a separate species.[14]

Here we present the use of machine-learned cluster expansions to computationally screen nanocatalysts of experimentally relevant sizes and identify those that are expected to have high activity. We demonstrate this approach on Pt–Ni nanoparticle catalysts for the oxygen reduction reaction (ORR), which have been extensively studied as promising catalysts in fuel cells.[5, 8, 33] We use the adsorption energy of OH as a descriptor of catalytic activity, as it has been shown to be an accurate descriptor,[34, 35] and in operating conditions OH is likely to be the most prevalent species on the alloy surface.[36] By explicitly including OH in the cluster expansion we realistically account for adsorbate-adsorbate interactions (See Methods). Catalytic activity is then predicted using kinetic Monte Carlo (KMC)[37, 38] simulations to calculate the turnover frequencies on all surface sites. Applying this approach to particles over a range of compositions and sizes yields catalytic activity maps for the ORR that indicate the optimal size, composition, and phase of the Pt–Ni nanoparticles, an important step towards the rational design of alloy nanocatalysts.

Results and Discussions

We start by validating our approach for predicting activities against experimental data. Experimentally, the measured specific and mass activities of Pt–Ni nanocatalysts are usually referenced to those of state-of-the-art commercial Pt/C.[3, 5, 15] To simulate this reference state, we have calculated size-weighted activity averages according to the diameter length distribution of commercial Pt/C used in our previous work (Table S2).[15] Based on the Wulff construction of Pt[14], we chose a truncated octahedron as the shape of Pt nanoparticles. Our KMC simulations predict the specific activity of the Pt(111) surface (Table S3) to be about 3.8 times relative to that of commercial Pt/C, which is in good agreement with experiments (5 – 10 times).[39, 40] We further validated our approach for predicting catalytic activities by comparing experimentally measured and KMC-predicted activities for two representative Pt–Ni octahedral particles (**Table 1**).[3, 15] The simulated structures of these particles were matched to experimental data as described in references 3, 15. The comparison suggests that our approach slightly overestimates the activities of the Pt–Ni nanoparticles, relative to Pt/C, by a factor of about 1.3 – 1.7. One possible reason for this overestimation is the underestimation of the activity of the Pt/C reference state, which may be due to the limited number of Pt particles used to estimate the size distribution of commercial Pt/C.[15] If the estimated size distribution of commercial Pt/C[15] is too heavily weighted towards small particles, the activity of the Pt/C reference state would be underestimated as the specific activity of Pt particles increases as a function of size (Table S2). Another possible source of error is the uncertainty of the peak position of Sabatier volcano plot, combined with errors inherent in DFT when calculating adsorption energies.[41] The exact value of the peak position of volcano plot is not well defined, and this uncertainty exponentially affects the predicted specific activity of Pt particles.[41] For example, if the peak position relative to calculated DFT values were shifted 10 meV to the left, the predicted specific activity of Pt/C would increase by a factor of about 1.5. More details on the specific activities of the Pt(111) surface and representative Pt–Ni(111) surfaces are provided in the Supporting Information (Table S3, and Figure S4 and S5).

Table 1. Validation of the approach for predicting activities of alloy nanoparticles. Comparison of the experimentally measured and KMC predicted specific and mass activities of two representative Pt–Ni octahedral particles. “before KMC” and “after KMC” mean before and after the simulation of Ni dissolution, respectively. The specific and mass activities were predicted on the snapshots of Pt–Ni particles after KMC (Ni dissolution). The experimental and predicted values are referenced to those of commercial Pt/C, respectively.

References	Pt–Ni octahedral particles		specific activity based on H_{upd}		mass activity	
	before KMC	after KMC	experiment	prediction	experiment	prediction
Jia et al.[15]	$Pt_{4495}Ni_{1680}$	$Pt_{4495}Ni_{895}$	10	16.90	6.88	11.03
Cao et al.[3]	$Pt_{4045}Ni_{2130}$	$Pt_{4045}Ni_{1078}$	13.33	17.65	9.29	12.67

To predict the catalytic activity of a nanoparticle it is first necessary to predict the nanoparticle structure. Pt–Ni nanoparticles used as ORR catalysts in proton exchange membrane (PEM) fuel cells typically start as disordered Pt–Ni solid solutions that achieve a Pt-rich shell through an activation process[3, 15] which is usually done by performing cyclic voltammetry (CV) in N_2-saturated 0.1 M $HClO_4$.[2, 3, 15] Under such acidic treatment, surface Ni oxides will dissolve and surface Pt/Ni atoms will migrate.[3, 15 42] To construct realistic nanoparticle structures, we initialize the particle as a fully disordered solid solution and simulate the activation process using KMC simulations that account for the presence of OH adsorbates, as described in our previous work.[3, 15] This approach has been shown to yield activated particles that agree well with experiments[3], but it does not fully account for possible additional dissolution and restructuring that may occur over the much longer time scales of the catalyst lifetime.[4, 5, 43, 44] We predict 6175-atom (~5.5 nm) nanoparticles with initial (pre-activated) Ni compositions of 40%, 30%, 20% and 10% lose about 40.0%, 34.9%, 31.2% and 28.0% of their Ni, respectively (Figure S6).

Once we have predicted the structure of a nanoparticle, we evaluate catalytic activities by using KMC to estimate the turnover frequency for each adsorbed OH. Specific and mass activities are then calculated by dividing the sum of turnover frequencies by the number of surface Pt atoms and the number of total Pt atoms, respectively. We construct catalytic activity maps (**Figure 1**) by repeating this process on a grid with respect to composition and particle edge length (as determined by the pre-activated particles). At each point on this grid, we sample 10 structures to reduce noise introduced by the stochastic determination of the nanoparticle structure. The resulting catalytic activity maps for Pt–Ni octahedral nanoparticles (**Figure 1**) reveal that specific activity increases with particle edge length and starts to plateau at an edge length of about 5.5 nm, reaching a maximal value of about 28 times that of Pt/C when the initial (pre-activated) nanoparticle has a composition of about $Pt_{0.85}Ni_{0.15}$ (**Figure 1**a). The mass activity is optimized at a composition of about $Pt_{0.8}Ni_{0.2}$ and an edge length of 3.3 nm – 3.8 nm (**Figure 1**b).

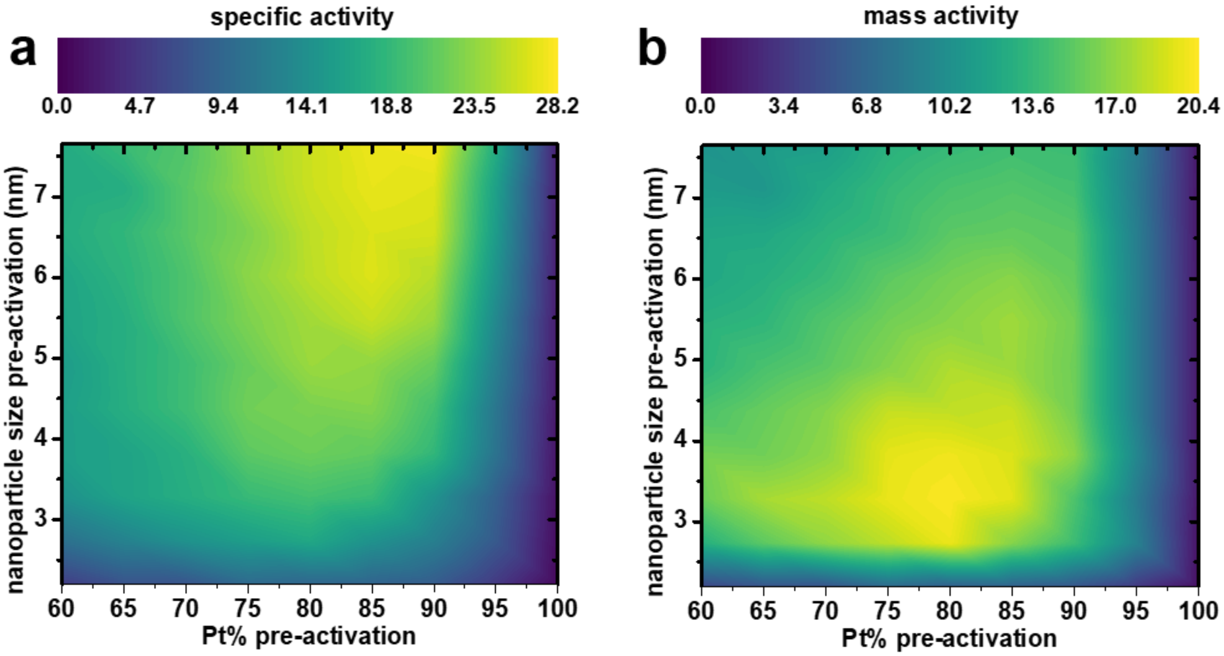

Figure 1. Size-composition catalytic maps of disordered Pt–Ni nanoparticles. a Predicted specific activity of activated particles. **b** Predicted mass activity of activated particles. The x-axis is the Pt composition before KMC (pre-activation) with an increment of 5%, and the y-axis is the edge length before KMC. All specific and mass activity values are referenced to those of simulated commercial Pt/C (see details in section 5 of the Supporting Information).

Comparison of our calculations to experimental results is challenging as there have been few reports of systematic experimental studies on size and composition effects in Pt–Ni particles. Experimentally, the highest reported mass activity for Pt–Ni nanoparticles by Younan Xia et al.[45] is about 17 times that of Pt/C. This result was achieved on octahedral $Pt_{0.72}Ni_{0.28}$ particles with an edge length of about 9 nm, but results on other sizes and compositions were not reported in that work. The solvent used in the synthesis of the nanoparticles was found to change the mass activity by a factor of two, highlighting the importance of factors beyond size and composition in determining particle activity. Alonso-Vante et al. studied composition effects in nanoparticles with diameters of 2–3 nm.[46] The variation of particle size with composition among the samples complicates the analysis of mass activity, but specific activity was found to have a broad peak around a composition of about $Pt_{0.7}Ni_{0.3}$. This is consistent with our prediction for 3.3 nm particles, which shows broad peaks with maximal activity at a composition of around $Pt_{0.8}Ni_{0.2}$ and only slightly less activity at a composition of $Pt_{0.7}Ni_{0.3}$ (Figure S7a). More recently, 4.5–7.5 nm (in edge length) Pt–Ni nanoparticles with a pre-activated composition of $Pt_{0.6}Ni_{0.4}$ were reported by Zhang et al. to be more active than particles with a pre-activated composition of $Pt_{0.75}Ni_{0.25}$.[47] The highest mass activity for the $Pt_{0.6}Ni_{0.4}$ particles was observed to occur for particles with an edge length of 5.8 nm, whereas the mass activity of the $Pt_{0.75}Ni_{0.25}$ nanoparticles showed relatively little change with particle size and was maximized for the largest particles. On the other hand, for pure Pt small nanoparticles (~2–3 nm in diameter) have been shown to maximize mass activity.[48, 49]

The size and composition at which we predict catalytic activity to be maximized are similar to those observed experimentally, but the experimental results suggest that peak activity occurs for nanoparticles with initial compositions that are more Ni-rich than those predicted by our models. This difference can be partially explained by the amount of Ni dissolution in the particles. For example, Zhang found that $Pt_{0.6}Ni_{0.4}$ nanoparticles with an edge length between 4.5 nm and 8.0 nm lost about 60% of the Ni in the particle after activation, but $Pt_{0.75}Ni_{0.25}$ nanoparticles with an edge length between 4.5 nm and 7.5 nm only lost about 25%.[47] As a result, the post-activated nanoparticles evaluated experimentally had nearly the same composition regardless of their initial compositions. In contrast, for disordered particles with an edge length of 5.5 nm our simulations predict 40% Ni loss for $Pt_{0.6}Ni_{0.4}$ and 32% Ni loss for $Pt_{0.75}Ni_{0.25}$. Thus the post-activated $Pt_{0.6}Ni_{0.4}$ nanoparticle has more Ni than the post-activated $Pt_{0.75}Ni_{0.25}$ nanoparticle, which weakens OH adsorption and leads to lower catalytic activity (Figure S8). Maps of predicted specific and mass activities for Pt–Ni nanoparticles as a function of the post-activated composition of the nanoparticle are provided in Figure S9. It is also possible that the particles undergo additional structural evolution after activation[4, 5, 43, 44] that is not captured by our simulated activation process.

We have found that in pure Pt and Pt-rich (111) surfaces, density functional theory predicts sub-surface vacancies to be significantly more stable than surface vacancies, by about 0.5 – 1 eV (Table S4). We believe this is likely related to reports that DFT significantly underpredicts bulk vacancy formation energies in Pt.[50, 51] Fortunately, this inherent error of DFT is mitigated by using the cluster expansion, which predicts much smaller differences between surface and sub-surface vacancies (Table S4). This may be a feature common to local energy models, as similar behavior has been observed in interatomic potentials trained by DFT – for some metals (including Pt) they predict vacancy formation energies more accurately than DFT does.[52, 53] The nanoparticle structures generated by our KMC calculations had a concentration of sub-surface vacancies below flat (111) surfaces of about 0.1% (Figure S10a). Most of the sub-surface Pt vacancies exist in the 2nd layer of the activated disordered particles. If this concentration is too high due to errors inherent in DFT, the resulting over-stabilization of Pt-rich (111) surfaces provides a possible explanation for the apparent under-prediction of Ni dissolution. There is evidence that the initial Pt concentration in Pt–Ni particles is greater near the particle edges,[5, 8] which may also explain the discrepancy between our predictions and experimental results. To investigate this possibility, we ran simulations on disordered Pt–Ni particles initialized with different degrees of Pt-rich edges. This process is described in detail in section 11 of the Supporting Information. We observed little change in the composition that is predicted to maximize activity (Figure S11), indicating that the initial distribution of Pt and Ni atoms cannot fully explain the slight difference between our calculations and experiments.

The calculated catalytic activity maps provide insights into the atomic origins of catalytic activity trends for alloy nanoparticles. At a composition of $Pt_{0.85}Ni_{0.15}$, which is predicted to yield nearly optimal specific activity, the specific activity increases as the edge length increases from 2.1 nm to 5.5 nm, and then starts to plateau when the edge length is larger than 5.5 nm (**Figure 2**a). This behavior can be largely attributed to the fraction of surface Pt atoms that are at sites with a GCN larger than 6.667, denoted as Pt(111) sites (**Figure 2**a). The average turnover frequencies are predicted to be maximized at these sites (**Figure 3**b-e and **Figure 4**e), as sites with lower GCN are effectively poisoned by strongly bound *OH. Comparison of the adsorption energies and turnover frequencies for steady-state OH coverage with those on clean nanoparticles (Figure S12) indicates that interactions between adsorbed *OH systematically weaken the OH binding energies on Pt(111) sites and decreases the turnover frequency.

The fraction of Pt(111) sites on the surface reaches a plateau of about 0.72 at an edge length of about 5.5 nm (**Figure 2**a), with the remaining surface Pt atoms on edge sites, vertex sites, near step edges, or near sub-surface vacancies (**Figure 3**b). This is in contrast to the expected behavior for an octahedral particle, in which the fraction of (111) sites should increase monotonically with particle size (**Figure 2**d). This observation indicates that when the pre-activated edge length gets larger than about 5.5 nm, any size-dependent increase in the density of Pt(111) sites on the surface is offset by an increase in the density of step edges (or other defects) on the surfaces of activated particles (Figure S13). Other factors, such as the second-layer composition (Figure S13 and S14b, and Table S6) are not as well correlated with specific activity.

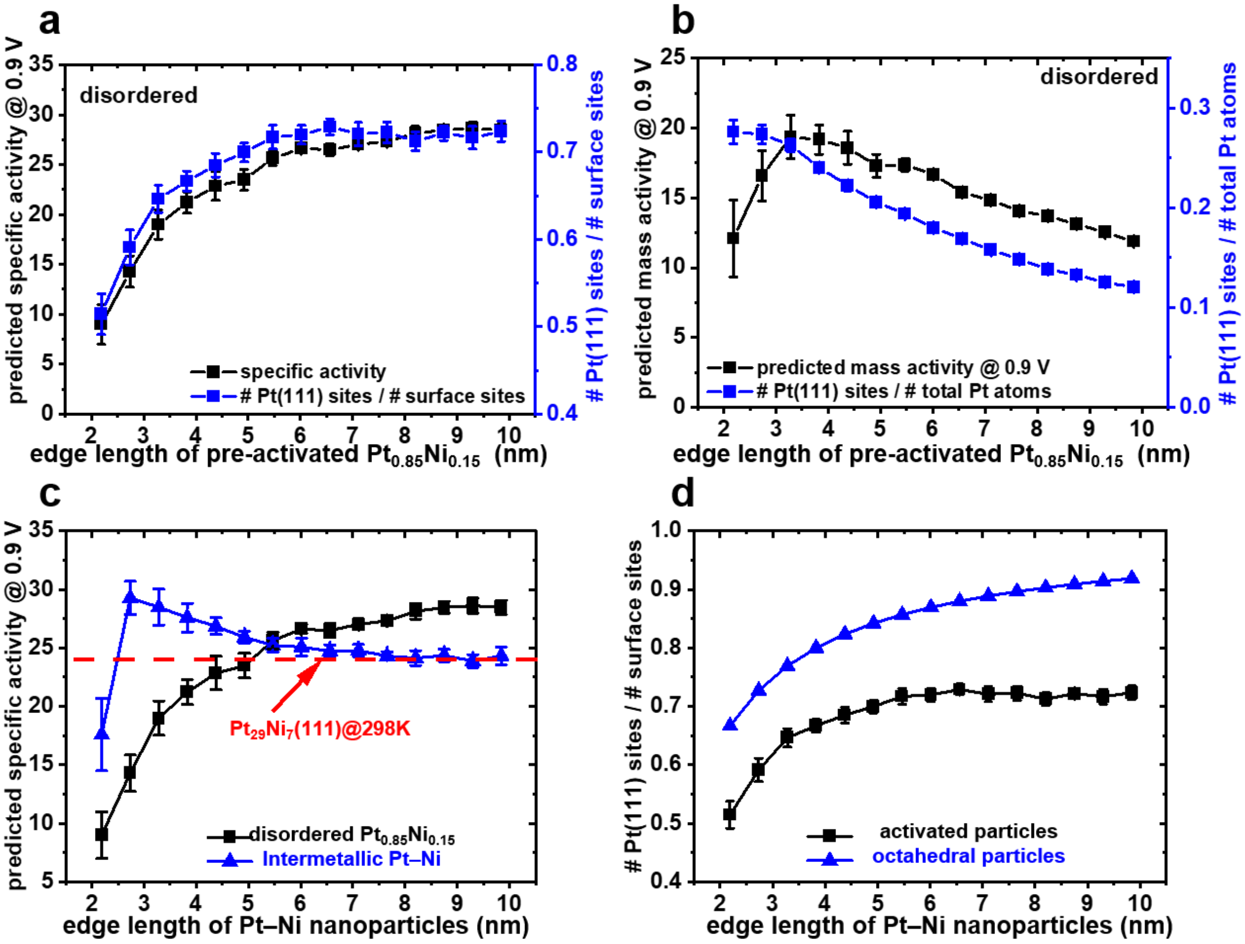

Figure 2. Size effect on specific and mass activities of Pt–Ni particles. a Predicted specific activity and ratio of the number of surface Pt(111) sites (GCN $\geqslant$ 6.667) to the number of total surface Pt atoms of disordered $Pt_{0.85}Ni_{0.15}$. **b** Predicted mass activity and ratio of the number of surface Pt(111) sites (GCN $\geqslant$ 6.667) to the number of total Pt atoms of disordered $Pt_{0.85}Ni_{0.15}$. **c** Predicted specific activity of disordered $Pt_{0.85}Ni_{0.15}$ and intermetallic Pt–Ni particles at the Pt and Ni chemical potentials that maximize the specific activity of 5.5 nm particles. The red line represents the $Pt_{29}Ni_7(111)$@298K surface with 100%, 75%, 75%, and 75% in the first, second, third, and fourth layers.[12] **d** Ratio of the number of surface Pt(111) atoms (GCN $\geqslant$ 6.667) to the number of total surface Pt atoms of activated disordered $Pt_{0.85}Ni_{0.15}$ (labeled as "activated particles") and octahedral particles. All specific activity and mass activity values are referenced to those of simulated commercial Pt/C.

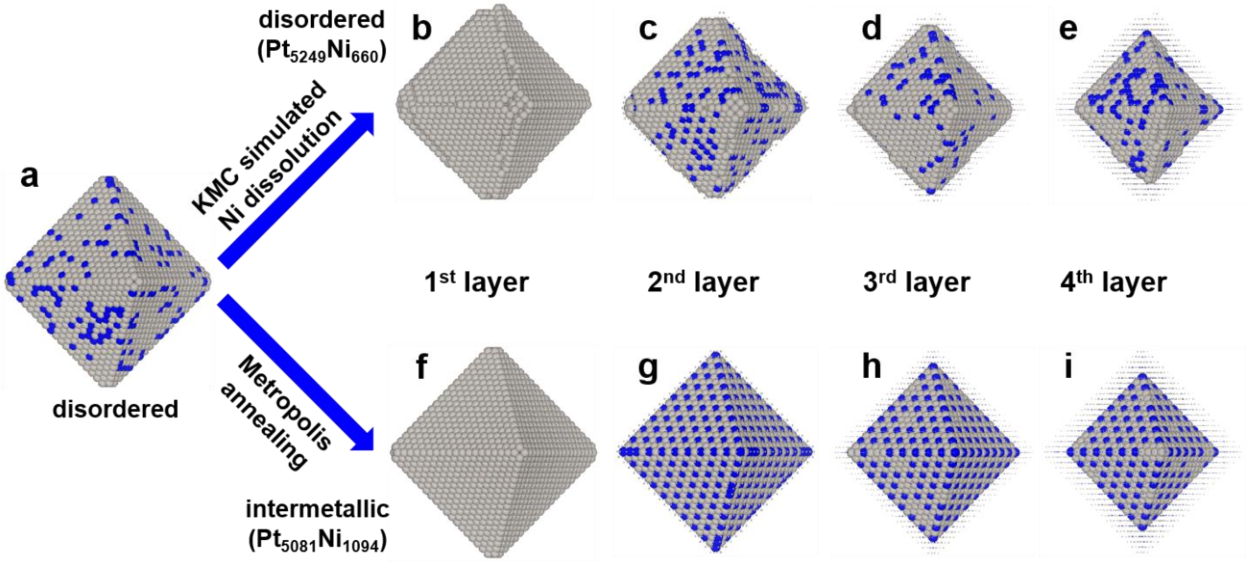

Figure 3. Layer-by-layer snapshots of disordered and intermetallic Pt–Ni particles. a A snapshot of disordered $Pt_{0.85}Ni_{0.15}$ nanoparticle with randomly occupied Pt/Ni atoms. **b, c, d, e** The first (**b**), second (**c**), third (**d**), and fourth (**e**) layers of a snapshot of activated disordered $Pt_{0.85}Ni_{0.15}$ nanoparticle after KMC simulation of Ni dissolution and Pt/Ni migration at 298 K. **f, g, h, i** The first (**f**), second (**g**), third (**h**), and fourth (**i**) layers of a snapshot of intermetallic $Pt_{0.82}Ni_{0.18}$ nanoparticle after Metropolis Monte Carlo simulation at 298 K.

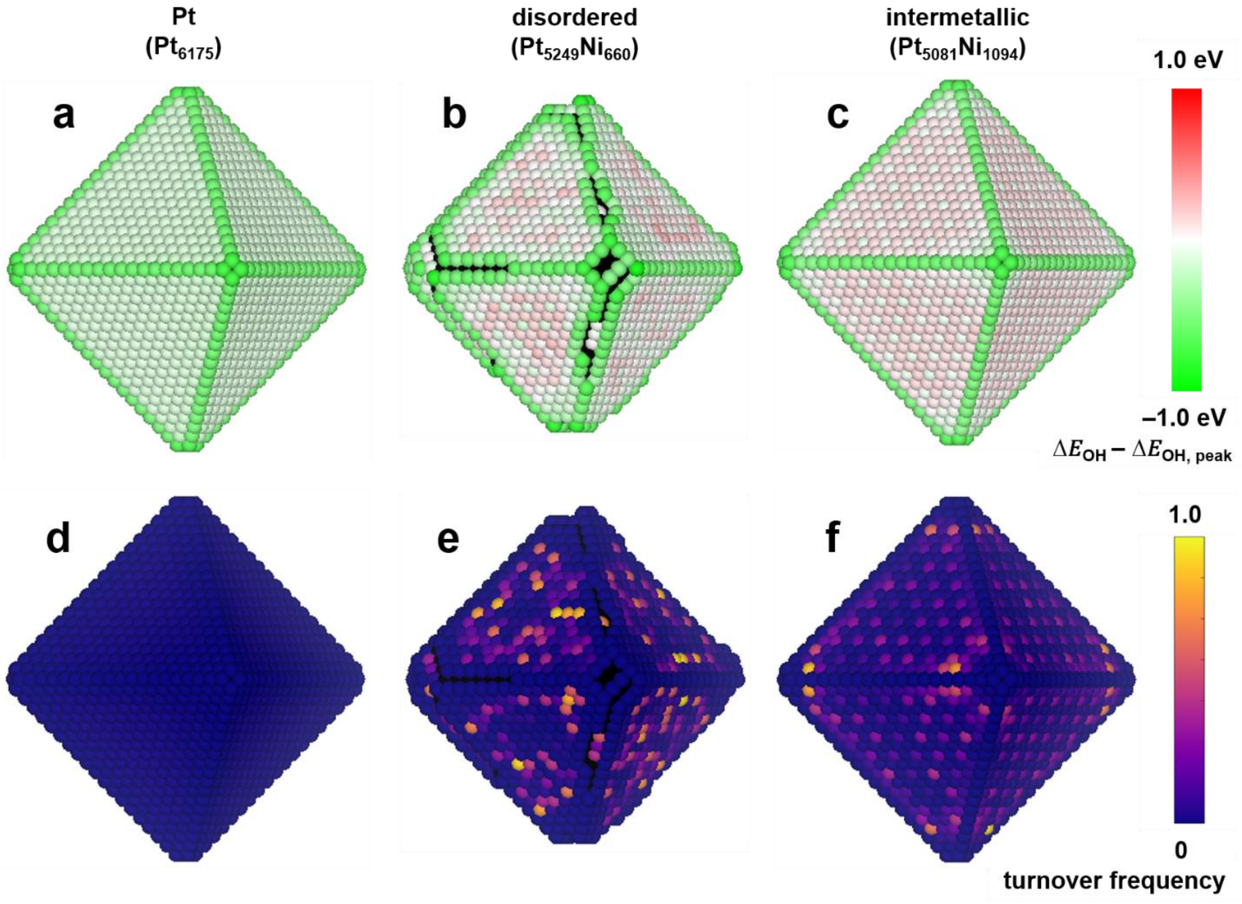

Figure 4. Predicted *OH binding energy and turnover frequency. a, b, c The average *OH binding energy on each surface site of three representative nanoparticles with an edge length of ~5.5 nm: Pt (**a**), disordered $Pt_{0.85}Ni_{0.15}$ in **Figure 3b-e** (**b**), and intermetallic $Pt_{0.82}Ni_{0.18}$ in **Figure 3f-i** (**c**). **d, e, f** The corresponding average turnover frequency on each site. Binding energies and turnover frequencies are referenced to those at the peak of the volcano plot and are averaged over the KMC recording steps. Corresponding histograms of binding energies and turnover frequencies are provided in Figure S23 and S24.

At the composition of $Pt_{0.85}Ni_{0.15}$, mass activity is predicted to increase as the edge length increases from 2.2 nm to 3.3 nm, and then it decreases as the edge length increases further (**Figure 2**b). The low mass activity at small sizes can be explained by the prediction that OH binding on Pt(111) sites becomes stronger at small particle sizes (Figure S15), consistent with DFT-calculated results that oxygen binding becomes stronger as the size of nanoparticle size decreases.[49] At larger sizes, the change in the *OH binding energy slows,[54] and the ratio of surface Pt(111) sites to the number of total Pt atoms becomes a more important factor in determining the size-dependent mass activity, leading to decreased mass activity (**Figure 2**b).

The highest reported specific activity for a Pt–Ni catalyst is on the extended $Pt_3Ni(111)$ surface [36], which is likely to be at least partially ordered in the thermodynamically stable $L1_2$ intermetallic phase.[55] We have thus also investigated an alternative hypothetical scenario, in which 2.2–9.9 nm octahedral nanoparticles are initialized with thermodynamically stable atomic ordering as determined using Metropolis Monte Carlo simulations[56] (described in detail in section 15 of the Supporting Information). The particles are estimated to maintain their octahedral shape due to their thermodynamic stability and the kinetic protection provided by the well-ordered Pt shell; this is supported by the fact that there is almost no Ni dissolution and shape change after running KMC on these intermetallic nanoparticles at 298 K. Within the chemical potential window in which bulk Pt_3Ni is stable, maximal specific and mass activities are achieved in intermetallic 6175-atom (~5.5 nm in the edge length) particles with a composition of about $Pt_{0.82}Ni_{0.18}$ (Figure S16a). These particles have an $L1_2$-ordered core (**Figure 3**f-i and Figure S17 and S18) and a Pt monolayer skin, in good agreement with the bulk phase diagram[55, 57] and previous calculations.[2, 13] Although intermetallic $Pt_{0.82}Ni_{0.18}$ particles and disordered $Pt_{0.85}Ni_{0.15}$ nanoparticles both have a Pt skin (**Figure 3**b, f), the activities of the intermetallic particles are much more sensitive to the overall particle composition than the activities of the disordered particles, as changes in the composition of the intermetallic particles largely occur through changes in the composition of the near-surface layers (Figure S17 and Table S7).

To investigate the size effect on specific and mass activities of intermetallic particles we set the chemical potential difference between Pt and Ni to that which maximizes activity in the 6175-

atom particles, resulting in an ordered $L1_2$ structure at all subsurface layers for particles with edge length larger than 3.3 nm (**Figure 3**f-i and Figure S18). For smaller particles, similar atomic structures have been observed but with slightly lower Pt content in sub-surface layers (Figure S19 and Table S8). The predicted specific activity and mass activity of intermetallic particles reaches a maximum value at about 2.7 nm edge length (**Figure 2**c and Figure S20). This peak can be explained by the fact that the average *OH binding energy on (111) sites for intermetallic particles increases with particle size and crosses over the volcano plot peak at about 2.7 nm (Figure S21). The predicted specific activity eventually converges to that of the extended $Pt_{29}Ni_7$(111) surface, which is predicted to be about 24 times that of commercial Pt/C (**Figure 2**c). Thus in the limit of large particle sizes the intermetallic nanoparticles are predicted to be less active than the most active activated disordered particles (**Figure 2**c). This observation can be explained by the fact that the second-layer Pt content is predicted to be lower in these intermetallic particles (Figure S19 and Table S8) than that in disordered particles (Figure S14 and Table S6) due to the dissolution of Ni atoms from the disordered particles. The relatively Pt-rich second layer in the disordered particles increases the strength of *OH adsorption and increases catalytic activity. This suggests that the additional stability that may be gained through the synthesis of intermetallic nanoparticles may come at the cost of slightly reduced activity.

We choose to model the octahedral shape for Pt–Ni nanoparticles because the (111) facets of the octahedra are highly active for the ORR. However one of the benefits of our approach is that it can be applied to a variety of shapes, reflecting the diversity of nanoparticle shapes that have been experimentally synthesized[5, 58-66] and theoretically investigated. [3, 15, 26-28, 59, 67] To investigate the effect of particle shape on catalytic activity, we have modeled the specific and mass activities of 6000-atom particles with octahedral, tetrahedral, spherical, and ellipsoidal shapes (Figure S22).

These calculations reveal that the (111)-rich tetrahedral and octahedral particles are predicted to have the highest activities, with the octahedral particle having slightly higher specific activity but the tetrahedral particle having higher mass activity.

Summary and Conclusions

Computational design of alloy nanocatalysts is challenging due to the need to predict nanoparticle structures, atomic ordering, adsorbate binding energies, adsorbate-adsorbate interactions, and kinetic evolution. We have demonstrated a novel approach using an accurate surrogate model trained on DFT calculations to address all of these challenges, enabling the construction of computationally-generated size-composition activity maps for Pt–Ni nanoparticles for the oxygen reduction reaction. The optimal size and composition predicted by these maps are close to those reported experimentally but slightly more Pt rich (before activation), which may be due to the underprediction of the amount of Ni that is lost to dissolution. One possible reason for this underprediction is that density functional theory predicts subsurface vacancies on Pt(111) to be about 1 eV more stable than surface vacancies. This surprising result is likely related to the well-established problems DFT has in predicting accurate Pt vacancy formation energies.

Our analysis of site-specific OH binding energy and turnover frequency on Pt–Ni nanoparticles demonstrates that surface sites with low generalized coordination number (GCN<6.667), such as edge and vertex sites, are highly inactive due to strong OH binding; while surface Pt(111) sites (GCN⩾6.667) are relatively more active. The fraction of these Pt(111) sites on the surfaces of activated nanoparticles does not grow as quickly as expected with increasing particle size, likely due to the presence of step edges and other defects. In the limit of large particle sizes, the activated, disordered nanoparticles are still predicted to have slightly higher specific activity than intermetallic Pt_3Ni with an $L1_2$-structured second layer due to lower Ni content in the second layer. At smaller particle sizes, well-ordered particles may have an advantage as they are predicted to be more resistant to Ni dissolution and thus may be better able to maintain the (111)-rich octahedral shape. However these predictions may not bear out in practice if Ni dissolution from either the disordered or intermetallic particle is greater than what we have modeled.

The comprehensive and systematic approach presented in this work has been demonstrated on Pt–Ni catalysts but is well suited to study other alloy systems (or multicomponent materials) and other catalytic reactions, especially those for which the binding energies of simple adsorbates have been established as accurate descriptors. The key to modeling these complex systems is to develop an accurate surrogate model, which has become increasingly feasible through advances in machine learning. Such models enable researchers to address problems with scale and complexity beyond those achievable with purely *ab initio* methods but with comparable accuracy. We believe this approach will be a valuable tool for computational chemists to conduct the rational design of alloy nanocatalysts.

Methods

Density functional theory (DFT) calculations

DFT calculations were run using the Vienna Ab Initio Simulation Package (VASP)[7] and the revised Perdew-Burke-Ernzerhof (RPBE) exchange-correlation functional.[68] The Ni, Pt_pv_GW, H_GW, and O_GW PBE projector-augmented wave (PAW)[69] potentials provided with VASP were used. VASP was run with accurate precision with a plane wave cutoff energy of 434 eV, at which the surface energy of 9-layer Pt(111) converges within 1 meV/Å^2 and the *OH binding energy on the top site of 9-layer Pt(111) converges within 10 meV. The Brillouin zone was sampled using a single *k*-point at the Γ point for DFT calculations of nanoparticles and gas-phase molecules. All DFT-calculated nanoparticles with fewer than 300 metal atoms were contained in a cubic cell with a lattice parameter of 28.8 Å, and Pt_{338} and Pt_{483} particles were contained in a cubic cell with a lattice parameter of 32.4 Å, to make sure that the vacuum layers between particles were larger than 10 Å. The vacuum layer for 9-layer Pt–Ni slabs was set as 9 equivalent layers of vacuum spacing (about 20 Å). For crystals the Brillouin zone was sampled using grids generated by the *k*-point grid server[70] with a minimum distance of 46.5 Å between real space lattice points for DFT calculations of slab and bulk materials. Spin polarization was taken into account in the calculations and the Methfessel–Paxton method[71] of order 2 was employed to determine electron occupancies with a smearing parameter of 0.2 eV. Real-space projectors were used to evaluate the non-local part of the PAW potential. The convergence criteria for the electronic self-consistent iteration and the ionic relaxation loop were set to be 10^{-4} eV and 10^{-3} eV, respectively.

Calculation of *OH binding energies

The *OH binding energy (ΔE_{OH}) on the surface site, *i*, of a nanoparticle was calculated as

$$\Delta E_{OH} = E_{DFT}\left(\mathrm{NP{+}k^{*}OH}\right) - E_{DFT}\left(\mathrm{NP{+}(k-1)^{*}OH}\right) + 0.5E_{DFT}\left(\mathrm{H_2}\right) - E_{DFT}\left(\mathrm{H_2O}\right), \tag{1}$$

where $E_{DFT}\left(\mathrm{NP{+}n^{*}OH}\right)$ is the DFT energy of the nanoparticle with *k* adsorbed *OH, $E_{DFT}\left(\mathrm{NP{+}(n-1)^{*}OH}\right)$ is the DFT energy of the same nanoparticle with one *OH on site *i* removed, and $E_{DFT}\left(\mathrm{H_2}\right)$ and $E_{DFT}\left(\mathrm{H_2O}\right)$ are the DFT energies of gas-phase H_2 and H_2O. By this definition, more negative values of ΔE_{OH} indicate stronger binding between *OH and the surface of the nanoparticle.

Cluster expansion construction

Cluster expansions are generalized Ising models commonly used to model atomic order,[72] in which the "spin" variables assigned to each site in an Ising model is replaced by "site" variables that indicate which species (or vacancy) is present at each site.[32] They are capable of very rapidly and accurately predicting the energies of different arrangements of atoms and vacancies, and they can be applied to bulk materials[73, 74], extended surfaces[12, 55], and nanoparticles.[3, 14] A detailed overview of the fundamentals and applications of cluster expansions, with a focus on nanoparticles and surfaces, is provided in reference 75.

The Pt–Ni–Vacancy cluster expansion built on a bulk fcc crystal lattice included 341 distinct cluster functions and was trained on 201 structures using the Bayesian approach[76] with a multivariate Gaussian prior distribution, resulting in a leave-one-out cross validation (LOO CV) error of 2.2 meV per atom relative to DFT. To predict OH binding energies on the surface of Pt–Ni nanoparticles with varied sizes, compositions, and shapes we constructed a quaternary Pt–Ni–OH@Pt–Vacancy cluster expansion on a bulk fcc crystal lattice. As catalytic activities were only calculated on structures that had a Pt skin, we were able to include OH in the cluster expansion by defining a dummy species representing a Pt atom bound to OH, which we refer to as OH@Pt. The Pt–Ni–OH@Pt–Vacancy cluster expansion included 1302 distinct cluster functions and was trained on 352 structures (including 144 Pt–Ni nanoparticles with adsorbed *OH) using the Bayesian approach, resulting in a LOO CV error of 2.3 meV per atom relative to DFT. To account for higher coverages of oxygen-related species on the Pt surface[77, 78], 14 structures with *OH coverages higher than 0.3 ML have been included in the training set, and the maximal *OH coverage in the training structures is 0.56 ML. The details of building two cluster expansions models in this work are provided in the part 1 of the Supporting Information.

KMC algorithm to predict nanoparticle structures

The Pt–Ni–Vacancy cluster expansion was used in kinetic Monte Carlo (KMC) simulations to predict the atomic structures of Pt–Ni nanoparticles after experimental CV activation. Detailed descriptions of this approach can be found in references 3, 15.

KMC algorithm to predict ORR activities

To evaluate the ORR specific activity of Pt–Ni nanoparticles, we used a standard "rejection-free" KMC algorithm[37, 38] to predict the turnover frequency on each site, here given by the *OH desorption rate. For each KMC step, the only allowed events were adsorption and desorption. We did not model surface diffusion, which should not affect the equilibrium *OH coverage and distribution. Only atoms with coordination numbers larger than 2 and smaller than 10 were considered to be surface atoms. The transition rate for each event is calculated as $e^{\frac{-E_a}{kT}}$, where E_a is the activation free energy for OH to desorb or adsorb. The free energy for adsorption was calculated as a function of the *OH binding energy to ensure that the turnover frequency was consistent with the right (adsorption-limited) leg of the Sabatier volcano as determined by the work of Norskov et al.[79, 80], and the free energy for desorption was similarly calculated to be consistent with the left (desorption-limited) leg. Additional details are provided in the Supporting Information.

ASSOCIATED CONTENT

Data Availability Statement

The cluster expansions were generated and applied using the matsci library, which is openly available at https://gitlab.com/muellergroup/matsci. The codes specifcic to this project, as well as the input and output files of fitting the cluster expansion parameters used to produce the results in this work are openly available in the GitLab repository at https://gitlab.com/muellergroup/AlloyNPs-CatalyticActivityMaps.

Supporting Information

Theoretical details of the cluster expansion, kinetic Monte Carlo (KMC) simulations to predict ORR activities, Metropolis Mote Carlo simulations, and other supplementary figures and tables are given.

AUTHOR INFORMATION

*Corresponding Author

Email: liangcao@zju.edu.cn; tmueller@jhu.edu

Author Contributions

The manuscript was written through contributions of all authors.

Notes

The authors declare no competing financial interests.

ACKNOWLEDGMENT

Tim Mueller acknowledges support from the Office of Naval Research under MURI award N00014-15-1-2681. Liang Cao acknowledges support from the National Natural Science Foundation of China under grant No. 22203072 and the Fundamental Research Funds for the Central Universities under award 226-2022-00167. Computational resources were provided by XSEDE through award DMR-140068, by the Maryland Advanced Research Computing Center (MARCC), and by AI + High Performance Computing Center of Institute of Computing Innovation, Zhejiang University (ZJU-ICI). Atomic-scale structural images were generated using VESTA.[81]

REFERENCES

(1) Kang, Y.; Snyder, J.; Chi, M.; Li, D.; More, K. L.; Markovic, N. M., et al. Multimetallic Core/Interlayer/Shell Nanostructures as Advanced Electrocatalysts. *Nano Lett.* **2014,** 14, 6361-6367.
(2) Huang, X.; Zhao, Z.; Cao, L.; Chen, Y.; Zhu, E.; Lin, Z., et al. High-performance transition metal–doped Pt3Ni octahedra for oxygen reduction reaction. *Science* **2015,** 348, 1230-1234.
(3) Cao, L.; Zhao, Z.; Liu, Z.; Gao, W.; Dai, S.; Gha, J., et al. Differential Surface Elemental Distribution Leads to Significantly Enhanced Stability of PtNi-Based ORR Catalysts. *Matter* **2019,** 1, 1567-1580.
(4) Beermann, V.; Gocyla, M.; Willinger, E.; Rudi, S.; Heggen, M.; Dunin-Borkowski, R. E., et al. Rh-Doped Pt–Ni Octahedral Nanoparticles: Understanding the Correlation between

Elemental Distribution, Oxygen Reduction Reaction, and Shape Stability. *Nano Lett.* **2016,** 16, 1719-1725.

(5) Cui, C.; Gan, L.; Heggen, M.; Rudi, S.; Strasser, P. Compositional Segregation in Shaped Pt Alloy Nanoparticles and Their Structural Behaviour during Electrocatalysis. *Nat. Mater.* **2013,** 12, 765-771.

(6) Kohn, W.; Sham, L. J. Self-Consistent Equations Including Exchange and Correlation Effects. *Phys. Rev.* **1965,** 140, A1133-A1138.

(7) Kresse, G.; Furthmueller, J. Efficient Iterative Schemes for Ab initio Total-Energy Calculations Using a Plane-Wave Basis Set. *Phys. Rev. B* **1996,** 54, 11169-11186.

(8) Gan, L.; Cui, C.; Heggen, M.; Dionigi, F.; Rudi, S.; Strasser, P. Element-Specific Anisotropic Growth of Shaped Platinum Alloy Nanocrystals. *Science* **2014,** 346, 1502-1506.

(9) Beermann, V.; Kühl, S.; Strasser, P. Tuning the Catalytic Oxygen Reduction Reaction Performance of Pt-Ni Octahedral Nanoparticles by Acid Treatments and Thermal Annealing. *J. Electrochem. Soc.* **2018,** 165, J3026-J3030.

(10) Chen, M.; Kumar, D.; Yi, C.-W.; Goodman, D. W. The Promotional Effect of Gold in Catalysis by Palladium-Gold. *Science* **2005,** 310, 291-293.

(11) Wang, Y.; Cao, L.; Libretto, N. J.; Li, X.; Li, C.; Wan, Y., et al. Ensemble Effect in Bimetallic Electrocatalysts for CO2 Reduction. *J. Am. Chem. Soc.* **2019,** 141, 16635-16642.

(12) Cao, L.; Mueller, T. Rational Design of Pt_3Ni Surface Structures for the Oxygen Reduction Reaction. *J. Phys. Chem. C* **2015,** 119, 17735-17747.

(13) Cao, L.; Mueller, T. Theoretical Insights into the Effects of Oxidation and Mo-Doping on the Structure and Stability of Pt-Ni Nanoparticles *Nano Lett.* **2016,** 16, 7748-7754.

(14) Li, C.; Raciti, D.; Pu, T.; Cao, L.; He, C.; Wang, C., et al. Improved Prediction of Nanoalloy Structures by the Explicit Inclusion of Adsorbates in Cluster Expansions. *J. Phys. Chem. C* **2018,** 122, 18040-18047.

(15) Jia, Q.; Zhao, Z.; Cao, L.; Li, J.; Ghoshal, S.; Davies, V., et al. Roles of Mo Surface Dopants in Enhancing the ORR Performance of Octahedral PtNi Nanoparticles. *Nano Lett.* **2018,** 18, 798-804.

(16) Li, C.; Nilson, T.; Cao, L.; Mueller, T. Predicting activation energies for vacancy-mediated diffusion in alloys using a transition-state cluster expansion. *Phys. Rev. Mater.* **2021,** 5, 013803.

(17) Curtarolo, S.; Morgan, D.; Ceder, G. Accuracy of ab initio methods in predicting the crystal structures of metals: A review of 80 binary alloys. *Calphad* **2005,** 29, 163-211.

(18) Verga, L. G.; Aarons, J.; Sarwar, M.; Thompsett, D.; Russell, A. E.; Skylaris, C. K. DFT calculation of oxygen adsorption on platinum nanoparticles: coverage and size effects. *Faraday Discuss.* **2018,** 208, 497-522.

(19) Tan, T. L.; Wang, L.-L.; Johnson, D. D.; Bai, K. A Comprehensive Search for Stable Pt-Pd Nanoalloy Configurations and Their Use as Tunable Catalysts. *Nano Lett.* **2012,** 12, 4875-4880.

(20) Yuge, K. Segregation of $Pt_{28}Rh_{27}$ Bimetallic Nanoparticles: A First-Principles Study. *J. Phys.: Condens. Matter* **2010,** 22, 245401.

(21) Wang, X.; Wang, Z.; Zhuang, T.-T.; Dinh, C.-T.; Li, J.; Nam, D.-H., et al. Efficient upgrading of CO to C3 fuel using asymmetric C-C coupling active sites. *Nat. Commun.* **2019,** 10, 5186.

(22) Chou, S.-W.; Lai, Y.-R.; Yang, Y. Y.; Tang, C.-Y.; Hayashi, M.; Chen, H.-C., et al. Uniform size and composition tuning of PtNi octahedra for systematic studies of oxygen reduction reactions. *J. Catal.* **2014,** 309, 343-350.

(23) Calle-Vallejo, F.; Tymoczko, J.; Colic, V.; Vu, Q. H.; Pohl, M. D.; Morgenstern, K., et al. Finding optimal surface sites on heterogeneous catalysts by counting nearest neighbors. *Science* **2015,** 350, 185-189.

(24) Calle-Vallejo, F.; Martínez, J. I.; García-Lastra, J. M.; Sautet, P.; Loffreda, D. Fast Prediction of Adsorption Properties for Platinum Nanocatalysts with Generalized Coordination Numbers. *Angew. Chem., Int. Ed.* **2014,** 53, 8316-8319.

(25) Ruck, M.; Bandarenka, A.; Calle-Vallejo, F.; Gagliardi, A. Oxygen Reduction Reaction: Rapid Prediction of Mass Activity of Nanostructured Platinum Electrocatalysts. *J. Phys. Chem. Lett.* **2018,** 9, 4463-4468.

(26) Rossi, K.; Asara, G. G.; Baletto, F. A genomic characterisation of monometallic nanoparticles. *Phys. Chem. Chem. Phys.* **2019,** 21, 4888-4898.

(27) Rück, M.; Bandarenka, A.; Calle-Vallejo, F.; Gagliardi, A. Fast identification of optimal pure platinum nanoparticle shapes and sizes for efficient oxygen electroreduction. *Nanoscale Adv.* **2019,** 1, 2901-2909.

(28) Rossi, K.; Asara, G. G.; Baletto, F. Structural Screening and Design of Platinum Nanosamples for Oxygen Reduction. *ACS Catal.* **2020,** 10, 3911-3920.

(29) Calle-Vallejo, F.; Bandarenka, A. S. Enabling Generalized Coordination Numbers to Describe Strain Effects. *ChemSusChem* **2018,** 11, 1824-1828.

(30) Jinnouchi, R.; Asahi, R. Predicting Catalytic Activity of Nanoparticles by a DFT-Aided Machine-Learning Algorithm. *J. Phys. Chem. Lett.* **2017,** 8, 4279-4283.

(31) Bartók, A. P.; Kondor, R.; Csányi, G. On representing chemical environments. *Phys. Rev. B* **2013,** 87, 184115.

(32) Sanchez, J. M.; Ducastelle, F.; Gratias, D. Generalized Cluster Description of Multicomponent Systems. *Phys. A (Amsterdam, Neth.)* **1984,** 128, 334-350.

(33) Zhao, Z.; Chen, C.; Liu, Z.; Huang, J.; Wu, M.; Liu, H., et al. Pt-Based Nanocrystal for Electrocatalytic Oxygen Reduction. *Adv. Mater.* **2019,** 31, 1808115.

(34) Viswanathan, V.; Hansen, H. A.; Rossmeisl, J.; Nørskov, J. K. Unifying the 2e– and 4e– Reduction of Oxygen on Metal Surfaces. *J. Phys. Chem. Lett.* **2012,** 3, 2948-2951.

(35) Viswanathan, V.; Hansen, H. A.; Rossmeisl, J.; Nørskov, J. K. Universality in Oxygen Reduction Electrocatalysis on Metal Surfaces. *ACS Catal.* **2012,** 2, 1654-1660.

(36) Stamenkovic, V. R.; Fowler, B.; Mun, B. S.; Wang, G.; Ross, P. N.; Lucas, C. A., et al. Improved Oxygen Reduction Activity on $Pt_3Ni(111)$ via Increased Surface Site Availability. *Science* **2007,** 315, 493-497.

(37) Schulze, T. P. Efficient kinetic Monte Carlo simulation. *J. Comput. Phys.* **2008,** 227, 2455-2462.

(38) Serebrinsky, S. A. Physical Time Scale in Kinetic Monte Carlo Simulations of Continuous-Time Markov Chains. *Phys. Rev. E* **2011,** 83, 037701.

(39) Gasteiger, H. A.; Kocha, S. S.; Sompalli, B.; Wagner, F. T. Activity Benchmarks and Requirements for Pt, Pt-Alloy, and non-Pt Oxygen Reduction Catalysts for PEMFCs. *Appl. Catal., B* **2005,** 56, 9-35.

(40) Paulus, U. A.; Wokaun, A.; Scherer, G. G.; Schmidt, T. J.; Stamenkovic, V.; Radmilovic, V., et al. Oxygen Reduction on Carbon-Supported Pt−Ni and Pt−Co Alloy Catalysts. *J. Phys. Chem. B* **2002,** 106, 4181-4191.

(41) Deshpande, S.; Kitchin, J. R.; Viswanathan, V. Quantifying Uncertainty in Activity Volcano Relationships for Oxygen Reduction Reaction. *ACS Catal.* **2016,** 6, 5251-5259.

(42) Menning, C. A.; Chen, J. G. Regenerating Pt–3d–Pt model electrocatalysts through oxidation–reduction cycles monitored at atmospheric pressure. *J. Power Sources* **2010,** 195, 3140-3144.

(43) Dionigi, F.; Weber, C. C.; Primbs, M.; Gocyla, M.; Bonastre, A. M.; Spöri, C., et al. Controlling Near-Surface Ni Composition in Octahedral PtNi(Mo) Nanoparticles by Mo Doping for a Highly Active Oxygen Reduction Reaction Catalyst. *Nano Lett.* **2019,** 19, 6876-6885.

(44) Polani, S.; MacArthur, K. E.; Klingenhof, M.; Wang, X.; Paciok, P.; Pan, L., et al. Size and Composition Dependence of Oxygen Reduction Reaction Catalytic Activities of Mo-Doped PtNi/C Octahedral Nanocrystals. *ACS Catal.* **2021,** 11, 11407-11415.

(45) Choi, S.-I.; Xie, S.; Shao, M.; Odell, J. H.; Lu, N.; Peng, H.-C., et al. Synthesis and Characterization of 9 nm Pt–Ni Octahedra with a Record High Activity of 3.3 A/mgPt for the Oxygen Reduction Reaction. *Nano Lett.* **2013,** 13, 3420-3425.

(46) Yang, H.; Vogel, W.; Lamy, C.; Alonso-Vante, N. Structure and Electrocatalytic Activity of Carbon-Supported Pt−Ni Alloy Nanoparticles Toward the Oxygen Reduction Reaction. *J. Phys. Chem. B* **2004,** 108, 11024-11034.

(47) Zhang, C.; Hwang, S. Y.; Peng, Z. Size-dependent oxygen reduction property of octahedral Pt–Ni nanoparticle electrocatalysts. *J. Mater. Chem. A* **2014,** 2, 19778-19787.

(48) Perez-Alonso, F. J.; McCarthy, D. N.; Nierhoff, A.; Hernandez-Fernandez, P.; Strebel, C.; Stephens, I. E. L., et al. The Effect of Size on the Oxygen Electroreduction Activity of Mass-Selected Platinum Nanoparticles. *Angew. Chem., Int. Ed.* **2012,** 51, 4641-4643.

(49) Shao, M.; Peles, A.; Shoemaker, K. Electrocatalysis on Platinum Nanoparticles: Particle Size Effect on Oxygen Reduction Reaction Activity. *Nano Lett.* **2011,** 11, 3714-3719.

(50) Mattsson, T. R.; Mattsson, A. E. Calculating the vacancy formation energy in metals: Pt, Pd, and Mo. *Phys. Rev. B* **2002,** 66, 214110.

(51) Nazarov, R.; Hickel, T.; Neugebauer, J. Vacancy formation energies in fcc metals: Influence of exchange-correlation functionals and correction schemes. *Phys. Rev. B* **2012,** 85, 144118.

(52) O'Brien, C. J.; Barr, C. M.; Price, P. M.; Hattar, K.; Foiles, S. M. Grain boundary phase transformations in PtAu and relevance to thermal stabilization of bulk nanocrystalline metals. *J. Mater. Sci.* **2018,** 53, 2911-2927.

(53) Alberto, H.; Tim, M. Generalizability of Functional Forms for Interatomic Potential Models Discovered by Symbolic Regression. *ArXiv* **2022**, arXiv:2210.15124.

(54) Leontyev, I. N.; Kuriganova, A. B.; Leontyev, N. G.; Hennet, L.; Rakhmatullin, A.; Smirnova, N. V., et al. Size dependence of the lattice parameters of carbon supported platinum nanoparticles: X-ray diffraction analysis and theoretical considerations. *RSC Adv.* **2014,** 4, 35959-35965.

(55) Cao, L.; Niu, L.; Mueller, T. Computationally generated maps of surface structures and catalytic activities for alloy phase diagrams. *Proc. Natl. Acad. Sci. U. S. A.* **2019,** 116, 22044-22051.

(56) Metropolis, N.; Rosenbluth, A. W.; Rosenbluth, M. N.; Teller, A. H.; Teller, E. Equation of State Calculations by Fast Computing Machines. *J. Chem. Phys.* **1953,** 21, 1087-1092.

(57) Lu, X.-G.; Sundman, B.; A˚gren, J. Thermodynamic assessments of the Ni–Pt and Al–Ni–Pt systems. *Calphad* **2009,** 33, 450-456.

(58) Wang, C.; Chi, M.-F.; Li, D.-G.; Strmcnik, D.; van der Vliet, D.; Wang, G.-F., et al. Design and Synthesis of Bimetallic Electrocatalyst with Multilayered Pt-Skin Surfaces. *J. Am. Chem. Soc.* **2011,** 133, 14396-14403.

(59) Wang, C.; Chi, M.; Wang, G.; van der Vliet, D.; Li, D.; More, K., et al. Correlation between Surface Chemistry and Electrocatalytic Properties of Monodisperse Pt_xNi_{1-x} Nanoparticles. *Adv. Funct. Mater.* **2011,** 21, 147-152.

(60) Tian, X.; Zhao, X.; Su, Y.-Q.; Wang, L.; Wang, H.; Dang, D., et al. Engineering bunched Pt-Ni alloy nanocages for efficient oxygen reduction in practical fuel cells. *Science* **2019,** 366, 850-856.

(61) Wu, Y.; Wang, D.; Niu, Z.; Chen, P.; Zhou, G.; Li, Y. A Strategy for Designing a Concave Pt–Ni Alloy through Controllable Chemical Etching. *Angew. Chem., Int. Ed.* **2012,** 51, 12524-12528.

(62) Chen, C.; Kang, Y.; Huo, Z.; Zhu, Z.; Huang, W.; Xin, H. L., et al. Highly Crystalline Multimetallic Nanoframes with Three-Dimensional Electrocatalytic Surfaces. *Science* **2014,** 343, 1339-1343.

(63) Gan, L.; Heggen, M.; Cui, C.; Strasser, P. Thermal Facet Healing of Concave Octahedral Pt–Ni Nanoparticles Imaged in Situ at the Atomic Scale: Implications for the Rational Synthesis of Durable High-Performance ORR Electrocatalysts. *ACS Catal.* **2016,** 6, 692-695.

(64) Niu, Z.; Becknell, N.; Yu, Y.; Kim, D.; Chen, C.; Kornienko, N., et al. Anisotropic phase segregation and migration of Pt in nanocrystals en route to nanoframe catalysts. *Nat. Mater.* **2016,** 15, 1188-1194.

(65) Wang, P.; Jiang, K.; Wang, G.; Yao, J.; Huang, X. Phase and Interface Engineering of Platinum–Nickel Nanowires for Efficient Electrochemical Hydrogen Evolution. *Angew. Chem., Int. Ed.* **2016,** 55, 12859-12863.

(66) Ding, J.; Bu, L.; Guo, S.; Zhao, Z.; Zhu, E.; Huang, Y., et al. Morphology and Phase Controlled Construction of Pt–Ni Nanostructures for Efficient Electrocatalysis. *Nano Lett.* **2016,** 16, 2762-2767.

(67) Callejas-Tovar, R.; Diaz, C. A.; de la Hoz, J. M. M.; Balbuena, P. B. Dealloying of platinum-based alloy catalysts: Kinetic Monte Carlo simulations. *Electrochim. Acta* **2013,** 101, 326-333.

(68) Hammer, B.; Hansen, L. B.; Nørskov, J. K. Improved adsorption energetics within density-functional theory using revised Perdew-Burke-Ernzerhof functionals. *Physical Review B* **1999,** 59, 7413.

(69) Blochl, P. E. Projector Augmented-Wave Method. *Phys. Rev. B* **1994,** 50, 17953-17979.

(70) Wisesa, P.; McGill, K. A.; Mueller, T. Efficient Generation of Generalized Monkhorst-Pack Grids through the Use of Informatics. *Phys. Rev. B* **2016,** 93, 155109.

(71) Methfessel, M.; Paxton, A. T. High-Precision Sampling for Brillouin-Zone Integration in Metals. *Phys. Rev. B* **1989,** 40, 3616-3621.

(72) Ising, E. Beitrag zur Theorie des Ferromagnetismus. *Zeitschrift für Physik* **1925,** 31, 253-258.

(73) Van de Walle, A.; Ceder, G. Automating First-Principles Phase Diagram Calculations. *J. Phase Equilib.* **2002,** 23, 348-359.

(74) Mueller, T.; Ceder, G. *Ab initio* Study of the Low-Temperature Phases of Lithium Imide. *Phys. Rev. B* **2010,** 82, 174307.

(75) Cao, L.; Li, C.; Mueller, T. The Use of Cluster Expansions To Predict the Structures and Properties of Surfaces and Nanostructured Materials. *J. Chem. Inf. Model.* **2018,** 58, 2401–2413.

(76) Mueller, T.; Ceder, G. Bayesian Approach to Cluster Expansions. *Phys. Rev. B* **2009,** 80, 024103.

(77) Casalongue, H. S.; Kaya, S.; Viswanathan, V.; Miller, D. J.; Friebel, D.; Hansen, H. A., et al. Direct observation of the oxygenated species during oxygen reduction on a platinum fuel cell cathode. *Nat. Commun.* **2013,** 4, 2817.

(78) Rossmeisl, J.; Karlberg, G. S.; Jaramillo, T.; Norskov, J. K. Steady State Oxygen Reduction and Cyclic Voltammetry. *Faraday Discuss.* **2008,** 140, 337-346.

(79) Rossmeisl, J.; Logadottir, A.; Norskov, J. K. Electrolysis of Water on (Oxidized) Metal Surfaces. *Chem. Phys.* **2005,** 319, 178-184.

(80) Karlberg, G. S.; Rossmeisl, J.; Norskov, J. K. Estimations of Electric Field Effects on the Oxygen Reduction Reaction based on the Density Functional Theory. *Phys. Chem. Chem. Phys.* **2007,** 9, 5158-5161.

(81) Momma, K.; Izumi, F. VESTA: A Three-Dimensional Visualization System for Electronic and Structural Analysis. *J. Appl. Crystallogr.* **2008,** 41, 653-658.

Supporting Information

Catalytic Activity Maps for Alloy Nanoparticles

Liang Cao[1,*], Tim Mueller[2,*]

[1]Institute of Catalysis, Department of Chemistry, Zhejiang University, Hangzhou, Zhejiang 310058, P. R. China

[2]Department of Materials Science and Engineering, Johns Hopkins University, Baltimore, Maryland 21218, United States

*Email: liangcao@zju.edu.cn; tmueller@jhu.edu

1. Cluster expansion

Cluster expansions are generalized Ising models commonly used to model atomic order,[1] in which the "spin" variables assigned to each site in an Ising model are replaced by "site" variables that indicate which species (or vacancy) is present at each site.[2, 3] Cluster expansions are capable of very rapidly and accurately predicting the properties of different arrangements of atoms and vacancies. A property (e.g., formation energy) of a material, which could be a bulk material[4, 5], extended surface[6, 7], or nanoparticle[8, 9], can be expressed as a function of these site variables:

$$F(\mathbf{s}) = V_0 + \sum_{clusters} V_{cluster} \prod_{i \in cluster} \Theta_{b,\mathrm{i}}\left(s_i\right) \qquad [1]$$

where the unknown coefficients, $V_{cluster}$, are known as effective cluster interactions (ECIs), s_i is the site variable at the i^{th} site, $\Theta_{b,i}$ is the b^{th} basis function for the i^{th} site, and V_0 is a constant term representing the ECI for the "empty" cluster. The sum is over clusters of sites, where the number of sites in a cluster may range from 1 to all the sites in the material. When all possible clusters are included in the expansion, the expansion in Eq. [1] is exact. In practice, the ECIs for clusters that contain a large number of sites or sites that are far apart are usually negligible, allowing for the expansion to be truncated to a sum with a finite number of ECIs with little loss of accuracy. The remaining ECIs accounting for many-body interactions are then fit to a set of training data (e.g., DFT-calculated formation energies of training structures).

To calculate the ORR activities on Pt–Ni nanoparticles, two cluster expansions models have been developed. The first one is a quaternary Pt–Ni–OH@Pt–Vacancy cluster expansion, which is used to explicitly predict *OH binding energies on the nanoparticle surface and account for the interactions among adsorbed *OH. The second one is the Pt–Ni–Vacancy cluster expansion, which is used to simulate the structural evolution of Pt–Ni nanoparticles using kinetic Monte Carlo and to predict the thermodynamically stable nanoparticles using Metropolis Monte Carlo.

1.1 Pt–Ni–OH@Pt–Vacancy cluster expansion on nanoparticles

The Pt–Ni–OH@Pt–Vacancy cluster expansion was built using an approach similar to one we previously used to build a Pt–Ni–Mo–Vacancy cluster expansion.[10-12] In the present work, we consider a surface Pt atom and a hydroxyl (OH) adsorbed on its top site as a single dummy species, which is expressed as *OH@Pt. The quaternary Pt–Ni–OH@Pt–Vacancy cluster expansion was generated on an fcc lattice in which each site could be occupied by *OH@Pt, nickel (Ni), platinum (Pt), or a vacancy. Site variable values of 0, 1, 2, and 3 respectively were assigned to these species. The constraint for the dummy species *OH@Pt is that it only can occupy surface sites. For each nanoparticle, atoms with coordination number (nearest-neighboring metal sites) larger than 2 and smaller than 10 are considered to be on surface sites. Pt and Ni Atoms were not permitted to have fewer than 3 nearest neighbors in Monte Carlo simulations. A discrete cosine basis was used to generate the cluster functions, where the b^{th} basis function of the site variable S is given by

$$\Theta_b = \begin{cases} 1 & \text{for b = 0} \\ \sqrt{2}\cos(\pi b(2\text{s} + 1) / 8) & \text{for b > 0} \end{cases}, \qquad [2]$$

for $b \in \{0,1,2,3\}$.

For the generation of training data, we reused all training structures that do not contain Mo atoms from the Pt–Ni–Mo–Vacancy cluster expansion[11], leading to an initial set of 151 random clean Pt–Ni particles. By randomly selecting from the pool of 151 clean particles, we created additional 95 random Pt–Ni particles with randomly decorated *OH on surface Pt atoms at varied coverages (68 particles with coverages between 0 and 0.1 ML, 23 particles with coverages between 0.1 ML and 0.2 ML, and 4 particles with coverages between 0.2 ML and 0.3 ML, respectively). All nanoparticles were generated under the constraint that there had to be more than 100 total Pt/Ni atoms in the nanoparticle, as we have found that the inclusion of smaller particles can lead to cluster expansions with poor predictive accuracy for multi-nanometer nanoparticles (probably due to quantum size effects). Nanoparticles that experienced significant reconstruction upon relaxation, defined as an atom traveling more than 75% the nearest-neighbor distance from its initial site, were excluded. All nanoparticles were contained in a cubic cell with a lattice parameter of 28.8

Å. The resulting set of random nanoparticles included 151 clean Pt-Ni nanoparticles without *OH and 95 Pt-Ni nanoparticles with *OH. To improve the accuracy of predicted ORR activities, we included 22 additional Pt–Ni nanoparticles with varied coverages and patterns of adsorbed *OH determined by KMC simulations of ORR activities (see details in section 2) and 7 9-layer Pt–Ni(111) surfaces into the training set. All DFT-calculated nanoparticles with fewer than 300 metal atoms were contained in a cubic cell with a lattice parameter of 28.8 Å, and Pt_{338} and Pt_{483} particles were contained in a cubic cell with a lattice parameter of 32.4 Å, to make sure that the vacuum layers between particles were larger than 10 Å. The vacuum layer for 9-layer slabs was set as 9 equivalent layers of vacuum spacing (about 20 Å).

In addition to these structures, the training data consisted of the pure elements Ni, and Pt in a bulk fcc crystal, vacuum (a lattice containing only vacant sites), and various low-energy structures predicted over the course of this research, for a total of 352 unique structures. These 352 unique training structures included 198 clean Pt–Ni nanoparticles, 144 Pt–Ni nanoparticles with *OH, 7 9-layer Pt–Ni(111) surfaces, 1 Pt bulk, 1 Ni bulk, and 1 vacuum structure. There are 100 structures with *OH coverages between 0 and 0.1 ML (included), 26 structures with *OH coverages between 0.1 ML and 0.2 ML (included), 9 structures with *OH coverages between 0.2 ML and 0.3 ML (included), 3 structures with *OH coverages between 0.3 ML and 0.4 ML (included), 7 structures with *OH coverages between 0.4 ML and 0.5 ML (included), and 4 structures with *OH coverages between 0.5 ML and 0.6 ML (included). There are 14 structures with *OH coverages higher than 0.3 ML in the training set, and the maximal *OH coverage in the training structures is 0.56 ML. To reduce the prediction error of the cluster expansion[13], the pure elements and vacuum were included twice in the training set. All energies of training set structures were calculated using density functional theory (DFT). Details of the DFT calculations are provided in the Methods section of main body. The effective cluster interactions (ECIs) of the cluster expansions were fit to the DFT-calculated formation energies of fully relaxed nanoparticles relative to the reference states of bulk fcc Ni, bulk fcc Pt, and $0.5E(H_2)–E(H_2O)$ for OH. The formation energy can be expressed as

$$FE_{DFT}\left(\mathrm{Pt_mNi_n}{}^{*}\mathrm{OH_k}\right) = E_{DFT}\left(\mathrm{Pt_mNi_n}{}^{*}\mathrm{OH_k}\right) - mE_{DFT}\left(\mathrm{Pt}\right) - nE_{DFT}\left(\mathrm{Ni}\right) + k\left[0.5E_{DFT}\left(\mathrm{H_2}\right) - E_{DFT}\left(\mathrm{H_2O}\right)\right], \quad [3]$$

where $E_{DFT}\left(\mathrm{Pt_mNi_n}{}^{*}\mathrm{OH_k}\right)$ is the total DFT energy of the Pt–Ni nanoparticle ($\mathrm{Pt_mNi_n}$) with k adsorbed *OH, $E_{DFT}\left(\mathrm{Pt}\right)$ and $E_{DFT}\left(\mathrm{Ni}\right)$ are the DFT energies of bulk fcc Pt and Ni per atom, and $E_{DFT}\left(\mathrm{H_2}\right)$ and $E_{DFT}\left(\mathrm{H_2O}\right)$ are the DFT energies of gas-phase H_2 and H_2O. Our choice of H_2(g) and H_2O(g) as reference states avoids potential errors in the calculation of the energy of O_2(g) and allows for more direct comparisons with previous calculations.[14]

The Pt–Ni–OH@Pt–Vacancy cluster expansion was truncated to include the empty cluster, the one-body (point) cluster, all 2-body clusters up to the seventh-nearest neighbor, all 3-body clusters up to the fifth-nearest neighbor, all 4-body clusters up to the third-nearest neighbor, and 5-, and 6-body clusters up to the second-nearest neighbor, for a total of 1302 symmetrically distinct cluster functions. The ECIs for these cluster functions were fit to the training data using the Bayesian approach with a multivariate Gaussian prior distribution.[15] The inverse of the covariance matrix for the prior, Λ, was diagonal, with elements given by

$$\lambda_{\alpha\alpha} = \begin{cases} 0 & \text{for } \mathrm{n}_\alpha = 0 \\ \lambda_1 & \text{for } \mathrm{n}_\alpha = 1, \\ \lambda_2(1+r_\alpha)^{\lambda_3} e^{\lambda_4 n_\alpha} & \text{for } \mathrm{n}_\alpha > 1 \end{cases} \quad [4]$$

where n_α is the number of sites in cluster function α, r_α is the maximum distance between sites, and the parameters λ_1, λ_2, λ_3, and λ_4 were determined by using a conjugate gradient algorithm to minimize the root mean square leave-one-out cross validation (RMS LOOCV) score, an estimate of prediction error.[4] The final values for these parameters were 1.000×10^{-8}, 9.414×10^{-12}, 4.286, and 2.986 respectively. The resulting cluster expansion had a RMS LOOCV error of 2.3 meV per atom relative to DFT calculations.

1.2 Pt–Ni–Vacancy cluster expansion on nanoparticles

The Pt–Ni–Vacancy cluster expansion was built by removing the dummy species (*OH@Pt: surface Pt atom adsorbed with *OH) from Pt–Ni–OH@Pt–Vacancy cluster expansion, removing the training structures containing adsorbed *OH, and removing the 9-layer Pt–Ni(111) slabs. The number of structures in the resulting training set is 201. The final values of fitting parameters in Eq. [4] were 1.000×10^{-8}, 9.414×10^{-9}, 4.286, and 2.986, respectively. The resulting cluster expansion had a RMS LOOCV error of 2.2 meV per atom relative to DFT calculations. This cluster expansion is used to simulate the structural evolution (Ni dissolution and Pt/Ni migration) during the experimental CV activation[8, 12] via kinetic Monte Carlo (KMC) as well as predict the thermodynamically stable Pt-Ni nanoparticles via Metropolis Monte Carlo.[10, 11]

2. Assessment of the accuracy of predicted *OH binding energies

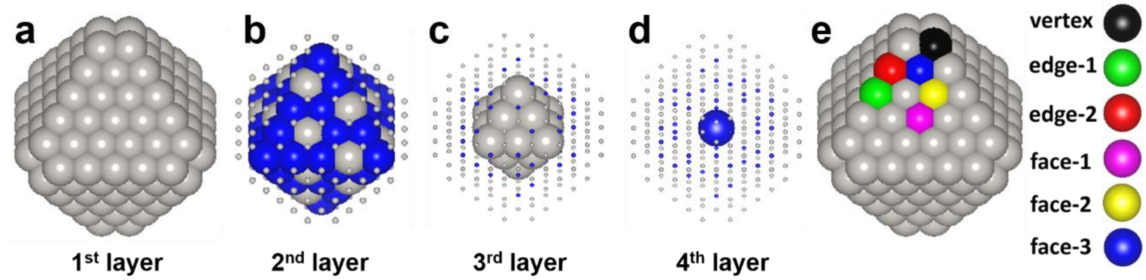

Figure S1. (a-d) The layer-by-layer atomic configuration of ground-state $Pt_{178}Ni_{47}$, which is predicted by the cluster expansion in vacuum (reported in our previous work[10, 11]). The 225-atom nanoparticle can be created by truncating one atom on each vertex of perfect octahedral 231-atom nanoparticle. (e) The six types of surface sites by their distinguished numbers of the nearest neighboring Pt/Ni atoms and the 2nd-nearest neighboring atoms.

Table S1. The comparison of DFT-calculated and CE-predicted *OH binding energy on varied nanoparticles with a dilute *OH coverage. The surface sites on $Pt_{178}Ni_{47}$ were defined in **Figure S1**e. and Pt_{225} was created by replacing all Ni atoms with Pt atoms. Pt_{79}, Pt_{140}, Pt_{225}, Pt_{338}, and Pt_{483} are octahedral nanoparticles with all vertex sites atoms truncated, where "surface-center" sites are the sites furthest to the edges. The generalized coordination number (GCN) was firstly introduced by Calle-Vallejo et al.[16, 17]

particle	surface site	CN	GCN	$\Delta E_{OH, DFT}$ /eV	$\Delta E_{OH, CE}$ /eV	diff /eV
Pt_{225}	face-1	9	7.5	1.082	0.979	0.103
	face-2	9	7.167	1.006	0.935	0.071
	face-3	9	6.667	0.992	0.902	0.090
	edge-1	7	5.167	0.660	0.640	0.020
	edge-2	7	5.083	0.653	0.614	0.039
	vertex	6	4.083	0.375	0.332	0.043
$Pt_{178}Ni_{47}$	face-1	9	7.5	1.322	1.323	–0.001
	face-2	9	7.167	1.293	1.200	0.093
	face-3	9	6.667	1.077	1.046	0.031
	edge-1	7	5.167	0.878	0.792	0.086
	edge-2	7	5.083	0.762	0.712	0.050
	vertex	6	4.083	0.458	0.459	–0.001
Pt_{79}	face-center	9	7.5	0.955	0.891	0.064
Pt_{140}	face-center	9	7.5	1.029	0.947	0.082
Pt_{225}	face-center	9	7.5	1.082	0.979	0.103
Pt_{338}	face-center	9	7.5	1.077	0.984	0.093
Pt_{483}	face-center	9	7.5	1.115	0.994	0.121

Note: To make sure that the vacuum layers between particles were larger than 10 Å, all DFT-calculated nanoparticles with less than 300 metal atoms were contained in a cubic cell with a lattice parameter of 28.8 Å, and Pt_{338} and Pt_{483} particles were contained in a cubic cell with a lattice parameter of 32.4 Å.

3. Sabatier volcano relating ΔE_{OH} to activation free energy

In this work, we assume the ORR occurs via the associative mechanism in acidic solution with an applied potential of 0.9 V (vs. the reversible hydrogen electrode, RHE) based on previous studies.[14, 18] The binding energies of three intermediate adsorbates (*OOH, *O and *OH) are linearly related.[19] The activation free energy along the reaction pathway (E_a) is correlated to oxygen binding energy (ΔE_O) through a Sabatier volcano plot.[6, 7, 18] This Sabatier volcano plot maps adsorption energies to activation free energies in a way that takes into account solvation effects (water-adsorbate interactions), zero-point energies, and entropy corrections.[18] The solvation effect has been treated by adding correction terms to the free energies of *OOH, *O and *OH. At an applied potential of 0.9 V, *OH is the most stable adsorbate on Pt–Ni surface. Thus we converted the Sabatier volcano as a function of oxygen binding energy to *OH binding energy by using the linear relationships among *OOH, *O, and *OH.[19] Thus the activation free energy is expressed as a function of the *OH binding energy (ΔE_{OH})

$$E_a = -\min(-0.297 + 1.0(\Delta E_{OH} - 1.153), -0.297 + 1.06(1.153 - \Delta E_{OH})). \qquad [5]$$

where all energies are given in eV and peak position of Sabatier volcano is $\Delta E_{OH,\,peak}$=1.115 eV. There is a difference between the peak position and OH binding energy on Pt(111) with a 1/4 ML coverage ($\Delta E_{OH,\,Pt(111)}$=1.035 eV), which is ~0.1 eV based on previous theoretical predictions[14, 20, 21], and ~0.135 eV based on experimental measurements.[22] The peak position ($\Delta E_{OH,\,peak}$=1.153 eV) was determined by adding the average of above theoretical and experimental differences, which is (0.1 + 0.135) / 2 ≈ 0.118 eV, to $\Delta E_{OH,\,Pt(111)}$.

To determine whether the linear relationships still hold on edge and face sites of a nanoparticle, we have performed DFT calculations on 225-atom particles (include Pt_{225} and $Pt_{178}Ni_{47}$, as shown in **Figure S1**). We find that the linear scaling still holds for both face(111) sites and edge sites only with slight differences between the intercepts and slopes. As shown in **Figure S2**, the fitted linear scaling between adsorption energies of *OOH and *OH including 12 different (111) face sites and 15 different edge sites is $\Delta E_{OOH} = 1.03\Delta E_{OH} + 2.99$, which is in good agreement with the one only including 12 (111) face sites ($\Delta E_{OOH} = 0.98\Delta E_{OH} + 3.06$), and the one only including 15 edge sites ($\Delta E_{OOH} = 1.05\Delta E_{OH} + 2.98$). These results indicate that the volcano plot built on the (111) slab model by Norskov et al. and his colleagues still works for octahedral particles.[18, 19]

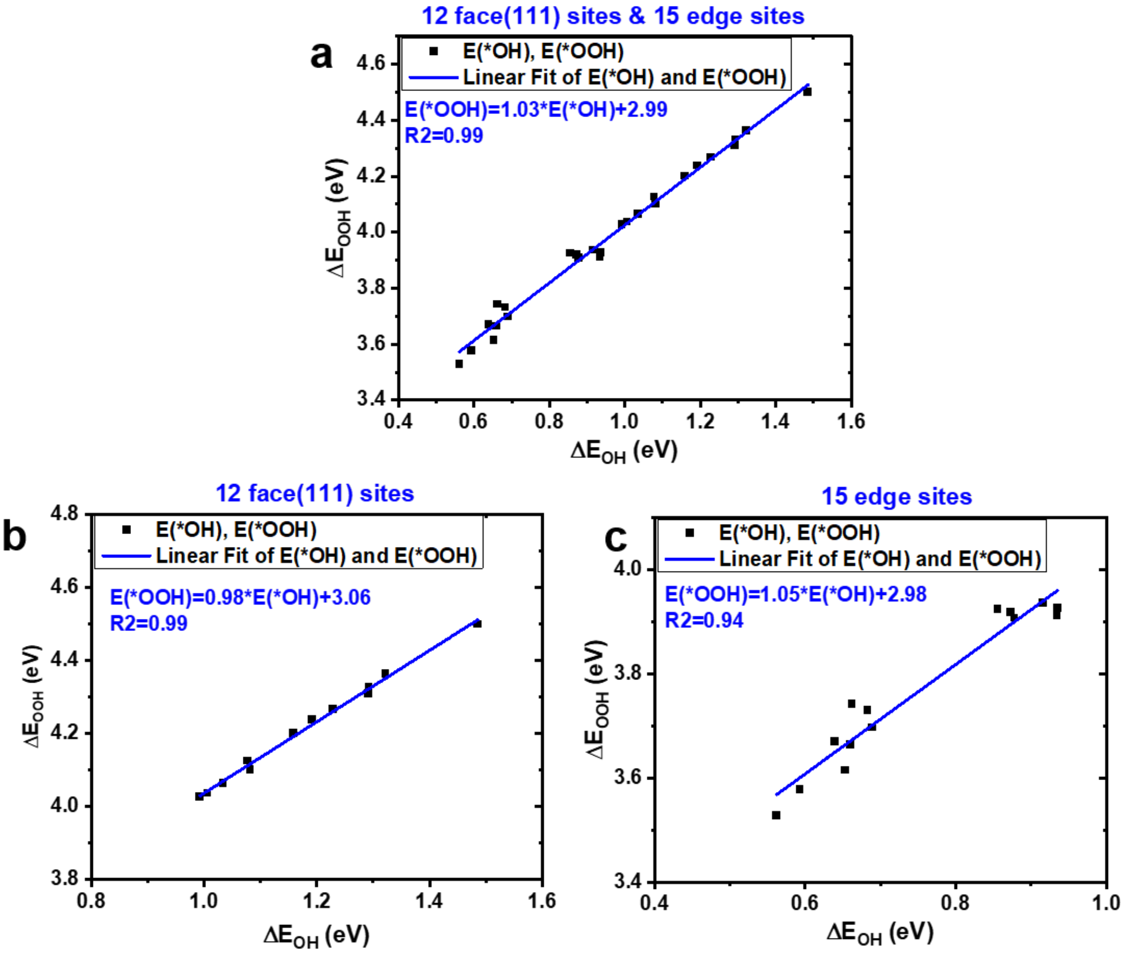

Figure S2. The linear relationship between DFT-calculated *OH and *OOH binding energies on (a) 12 (111) face sites and 15 edge sites, (b) just the 12 (111) face sites, (c) just the 15 edge sites of a 225-atom particles (including Pt_{225} and $Pt_{178}Ni_{47}$ as shown in **Figure S1**).

4. Kinetic Monte Carlo (KMC) simulation to predict ORR activities

To estimate ORR specific activity, we have developed an approach in which the turnover frequency at each site is determined through a KMC simulation. The site-specific turnover frequency is expressed as

$$\text{turnover frequency} = e^{-\frac{E_a}{kT}}, \tag{6}$$

where E_{α} is the activation free energy and calculated using the Sabatier volcano at varied *OH coverages.

This approach is similar to the one used in our previous work on Pt–Ni(111) surfaces with one monolayer of adsorbed *O/Vacancy.[7] We use a standard "rejection-free" KMC algorithm [23, 24] in which the only allowed transitions are adsorption and desorption. Each simulation was done on each independent nanoparticle, so the number of possible transition events for each KMC step is actually equal to the number of surface Pt atoms (i.e. 1596 for the intermetallic Pt_3Ni nanoparticle in **Figure 1**f). In this work, only surface atoms whose coordination number (nearest-neighboring Pt/Ni atoms) is larger than 2 and smaller than 10 are considered as surface atoms. The transition rates (or turnover frequencies) for the transition events were calculated as $e^{\frac{-\mathrm{E}_a}{\mathrm{kT}}}$.

Specifically, for an adsorption event,

$$\mathrm{E}_a = 0.297 + \max(0,\ 1.06(\Delta\mathrm{E}_{\mathrm{OH}} - 1.153)), \tag{7}$$

where 1.115 is the peak position ($\Delta E_{OH,\,peak}$=1.115 eV) of the volcano plot. For a desorption event,

$$\mathrm{E}_a = 0.297 + \max(0,\ 1.0(1.153 - \Delta\mathrm{E}_{\mathrm{OH}})). \tag{8}$$

The maximum of E_a for an adsorption and a desorption event reproduces the equation of Sabatier volcano (Eq. [5]). After each event, the total elapsed "KMC time" was incremented by

$$\Delta t_{KMC} = \left(\frac{1}{R_N}\right) * \ln\left(\frac{1}{u_1}\right) \tag{9}$$

where R_N is the total rate that sum all possible transition events, and u_1 is a uniform random number with $\mu_1 \in (0, 1]$. At the end of the run, the ORR specific activity (SA_{KMC}) was then calculated using

$$SA_{\mathrm{KMC}} = SA_0 \left(\frac{\mathrm{n(accepted\ desorption\ events)}}{t_{\mathrm{KMC\_record}}} \right) \tag{10}$$

where SA_0 is a prefactor, $\mathrm{n(accepted\ desorption\ events)}$ is the number of accepted *OH desorption events, and $t_{\mathrm{KMC\_record}}$ is the total "KMC time" of KMC recording steps. When SA_0 is the inverse of the number of adsorption sites on the surface of the studied nanoparticle (i.e. 1/1596 for the intermetallic Pt_3Ni nanoparticle in **Figure 1**f), then the KMC current agrees with the current calculated from the Sabatier volcano (Eq. [5]) in the limit of dilute coverage of *OH. The above specific activity (SA_{KMC}) can be converted to mass activity (MA_{KMC}) by multiplying the ratio of the number of surface Pt atoms ($N_{Pt,\,surface}$) to the number of total Pt atoms (N_{Pt}) for a particle.

$$\mathrm{S}A_{\mathrm{KMC}} = \frac{I}{N_{Pt,\,surface}} \tag{11}$$

$$MA_{\mathrm{KMC}} = \frac{I}{N_{Pt}} = \frac{\mathrm{S}A_{\mathrm{KMC}} \times N_{Pt,\,surface}}{N_{Pt}}, \tag{12}$$

where I is the hypothetical total current.

To determine the atomic structures, 10 different octahedral Pt–Ni nanoparticles with the same size and same Pt composition were randomly initialized, and 10 parallel KMC simulations of structural evolution (or Metropolis Monte Carlo simulations) were used to generate 10 different snapshots of activated disordered (or intermetallic) nanoparticles. To calculate the specific and mass activities, we ran a KMC simulation on each disordered or intermetallic nanoparticle. For each KMC simulation, the numbers of both equilibration steps and recording steps are 15 times the number of adsorption sites, and the predicted specific and mass activities and errors were average values and standard deviations (SA based on Eq. [10] and MA based on Eq. [12]) over 10 independent KMC runs on 10 nanoparticles. An example of *OH evolution on the surface of an activated 5.5-nm disordered $Pt_{0.85}Ni_{0.15}$ particle is given in **Figure S3**. The *OH coverage at edge sites (surface sites with GCN<6.667) dramatically increases as the normalized KMC time increases from 0 to 0.05 and reaches the plateau of 0.97 ML. It reaches this plateau well before the end of the equilibration period (the midpoint of the total simulation).

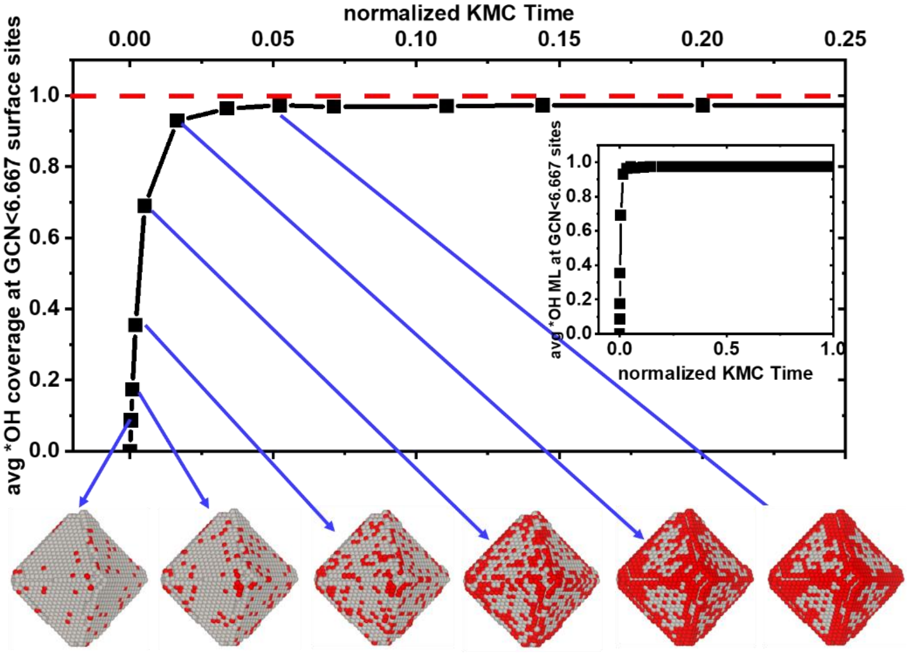

normalized KMC Time					
0.0004	0.0009	0.0020	0.0051	0.0165	0.0524
average *OH coverage at CN<9 surface sites					
0.09	0.17	0.35	0.69	0.93	0.97

Figure S3. The KMC-predicted average *OH coverage (ML) at GCN<6.667 surface sites as a function of normalized KMC time. The total number of KMC iterations is 43200, which is 30 times the number of adsorption sites (1440). Snapshots of the nanoparticle structures are shown on the bottom row. The grey and red spheres represent Pt atoms and *OH adsorbed on surface Pt atoms, respectively. The inset is over the course of the entire KMC simulation.

5. Benchmark of ORR activities of commercial Pt/C

The definitions of specific activity (SA) and mass activity (MA) for a single Pt–Ni particle are expressed in Eq. [11] and Eq. [12]. To simulate the SA and MA of state-of-the-art commercial Pt/C, we chose a cuboctahedron as the shape of pure Pt nanoparticles based on the Wulff construction of Pt demonstrated in the work of Li et al.[9] The size (in diameter length) distribution of commercial Pt/C (**Table S2**) was pulled from our previous work.[12] The weighted average values of SA (3.04E-08) and MA (1.21E-08) for commercial Pt/C were calculated according to the following expressions.

$$\langle SA \rangle = \frac{I}{N_{Pt,\,surface}} = \frac{\sum_i I_i \times p_i}{\sum_i n_{Pt,\,surface,\,i} \times p_i} = \frac{\sum_i (SA_i \times n_{Pt,\,surface,\,i}) \times p_i}{\sum_i n_{Pt,\,surface,\,i} \times p_i}; \qquad [13]$$

$$\langle MA \rangle = \frac{I}{N_{Pt}} = \frac{\sum_i I_i \times p_i}{\sum_i n_{Pt,\,i} \times p_i} = \frac{\sum_i (SA_i \times n_{Pt,\,surface,\,i}) \times p_i}{\sum_i n_{Pt,\,i} \times p_i}. \qquad [14]$$

As shown in **Table S2**, p_i is the percentage of particles listed for a specific diameter d is the total percentage of particles with the diameters in the range of d±0.275 nm, and $n_{Pt,\,surface,\,i}$ and $n_{Pt,\,i}$ are the number of surface Pt atoms and the number of all Pt atoms.

Table S2. The simulated specific activity (SA) and mass activity (MA) of commercial Pt/C with the size in diameter (d) distribution of commercial Pt/C pulled from our previous work.[12] The percentage of particles listed for a specific diameter d is the total percentage of particles with the diameters in the range of d±0.275 nm. The nanoparticles with the diameters smaller than 2 nm have not been counted because the KMC-predicted ORR activities are likely to be less accurate at such small sizes due to quantum finite-size effects. The values of SA_i were predicted using the KMC simulations.

cubo-octahedron	size in diameter (d)/nm	percentage (p_i)	SA_i	MA_i	$n_{Pt,surface,i}$	$n_{Pt,i}$
Pt_{5851}	5.504	0	6.97E-8	1.73E-8	1452	5851
Pt_{4249}	4.954	2.353	6.61E-8	1.79E-8	1148	4249
Pt_{3101}	4.403	1.176	5.40E-8	1.62E-8	930	3101
Pt_{2075}	3.853	5.882	4.78E-8	1.59E-8	690	2075
Pt_{1385}	3.302	14.118	3.54E-8	1.34E-8	524	1385
Pt_{807}	2.752	41.176	2.35E-8	1.01E-8	348	807
Pt_{459}	2.202	35.295	1.45E-8	7.39E-9	234	459
weighted average of SA			3.04E-8			
weighted average of MA				1.21E-8		

Using the Pt–Ni–OH@Pt–Vacancy cluster expansion, the predicted specific activity of Pt(111) on a 12×12 Pt(111) supercell is 1.15E-7 (**Table S3**), which is about 3.8 times that of commercial Pt/C (3.04E-8 in **Table S2**) and agrees well with experiments (5 – 10 times).[25, 26] The predicted specific activity of the theoretically identified ground state $Pt_{29}Ni_7$(111)[6] in equilibrium with bulk Pt_3Ni, which we will refer to as "$Pt_{29}Ni_7$(111)" (**Figure S4**a), is about 24.0 times that of commercial Pt/C (3.04E-8). The Pt_3Ni(111) catalyst (PNAS) 7-layer surface[7] and Pt_3Ni(111) catalyst (JPCC) 9-layer surface[6] (**Figure S5**) were cluster-expansion-predicted surfaces closely matching the layer-by-layer Pt compositions of the highly active Pt_3Ni(111) catalyst reported by Stamenkovic et al.[27]

Table S3. The KMC-predicted specific activities of 7-layer and 9-layer Pt–Ni(111) surfaces compared with the predicted ones of 9-layer Pt(111) and commercial Pt/C provided in **Table S2**. The highly active $Pt_3Ni(111)$ surface reported by Stamenkovic et al. is also included. The specific activity simulations of 7-layer, and 9-layer Pt–Ni(111) were conducted on a 12×12(111) supercell with a vacuum thickness of 11-layer, 9-layer Pt/Ni atoms, respectively.

prediction	SA_{KMC}	SA_{KMC} referenced to commercial Pt/C	SA_{KMC} referenced to Pt(111)
Pt(111)	1.15E-7	3.8	1
$Pt_{29}Ni_7(111)$	7.28E-7	24.0	6.3
$Pt_3Ni(111)$ catalyst (PNAS)	6.18E-07	20.3	5.4
$Pt_3Ni(111)$ catalyst (JPCC)	7.10E-07	23.4	6.2
$Pt_{25}Ni_{11}(111)$-a	1.22E-07	4.0	1.1
$Pt_{25}Ni_{11}(111)$-b	9.14E-10	0.03	0.01
experiment	SA (mA/cm^2)	SA referenced to commercial Pt/C	SA referenced to Pt(111)
$Pt_3Ni(111)$ reported by Stamenkovic at al.[27]	18	90	10

Note: $Pt_{25}Ni_{11}(111)$-a (**Figure S4**a) and $Pt_{25}Ni_{11}(111)$-b (**Figure S4**c) are 9-layer surfaces with a Pt-skin in the 1st layer and ordered Pt_3Ni in the 4th and 5th layers.[6] The 2nd and 3rd layers are 75% and 25% Pt for $Pt_{25}Ni_{11}(111)$-a, and 100% and zero Pt for $Pt_{25}Ni_{11}(111)$-b.

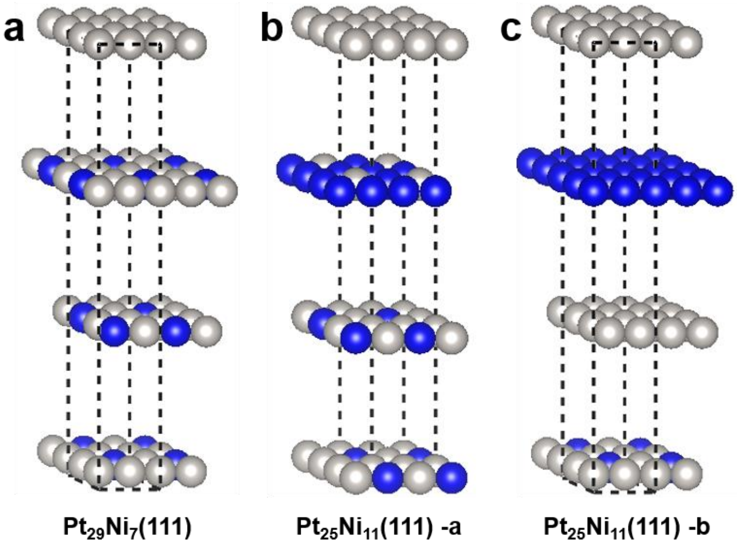

Figure S4. The top four layers of three symmetric 9-layer surfaces with a lattice parameter of intermetallic bulk Pt_3Ni. (a, c) ground state surfaces in equilibrium with bulk Pt_3Ni at 0 K predicted in our previous work[6]; (b) a dummy surface with 25%, 75%, and 75% Pt in the 2nd, 3rd, 4th layers, respectively. The grey and blue spheres are Pt and Ni atoms respectively.

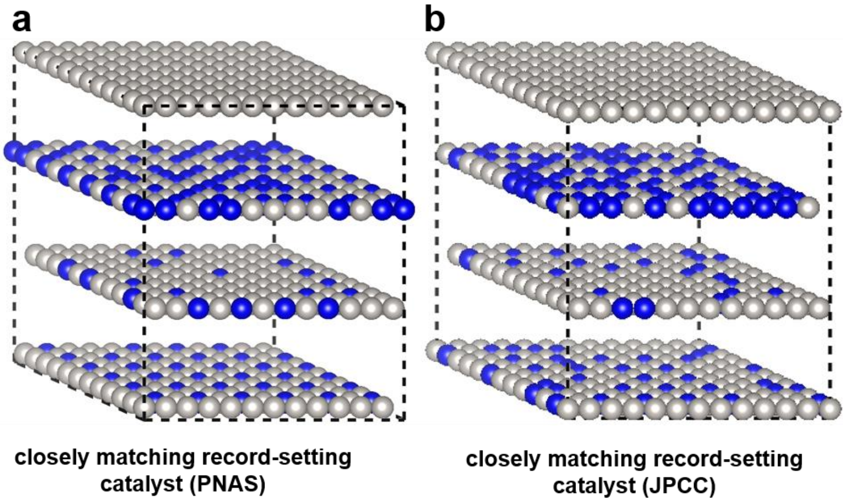

Figure S5. The top four layers of two snapshot slabs with a 12 × 12 (111) unit cell from Monte Carlo simulations. (a) a 7-layer snapshot[7] and (c) a 9-layer snapshot[6] matching the layer-by-layer Pt compositions of the highly active $Pt_3Ni(111)$ catalyst reported by Stamenkovic et al.[27] The grey and blue spheres are Pt and Ni atoms respectively.

6. Predicted Ni loss of activated disordered Pt–Ni nanoparticles

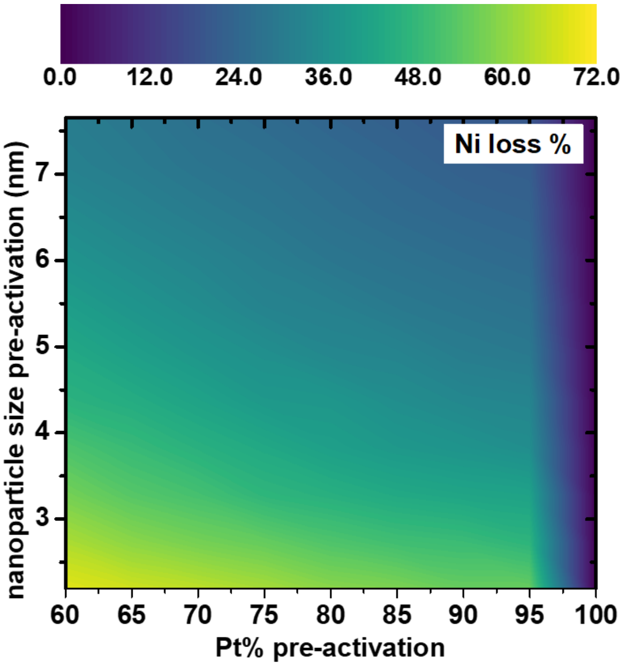

Figure S6. Predicted Ni loss of activated disordered Pt–Ni nanoparticles. The x-axis is the Pt composition after KMC with an increment of 5%, and the y-axis is the edge length before KMC (edge length). All specific and mass activity values are referenced to those of simulated commercial Pt/C.

7. Precited specific and mass activities of 3.3 nm disordered particles

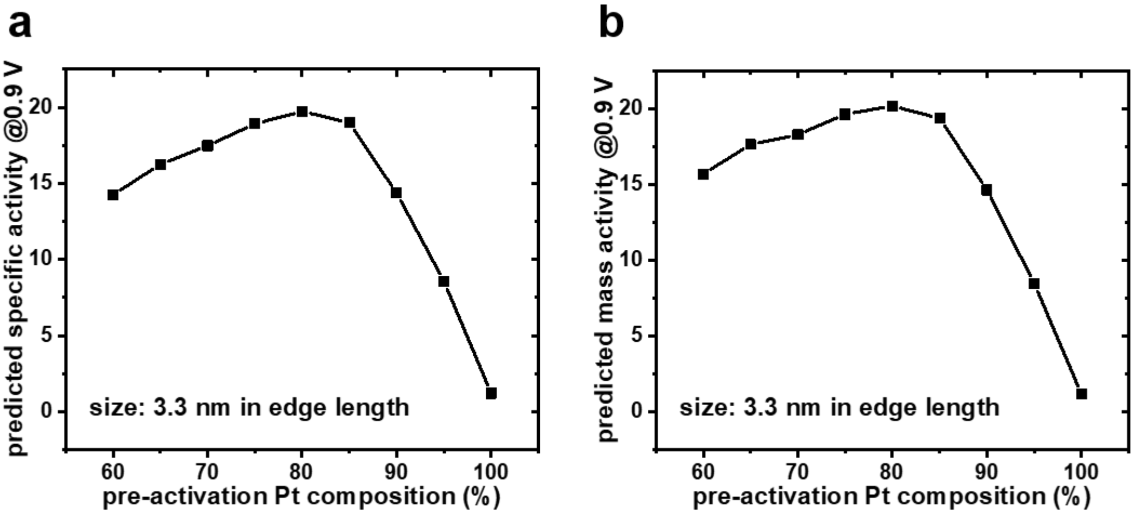

Figure S7. The predicted (a) specific activity and (b) mass activity of 3.3 nm activated disorder Pt–Ni particles as a function of pre-activation Pt composition. The values of activities are referenced to those of commercial Pt/C.

8. Predicted average *OH binding energies of post-activated disordered 6175-atom nanoparticles as a function of Pt composition

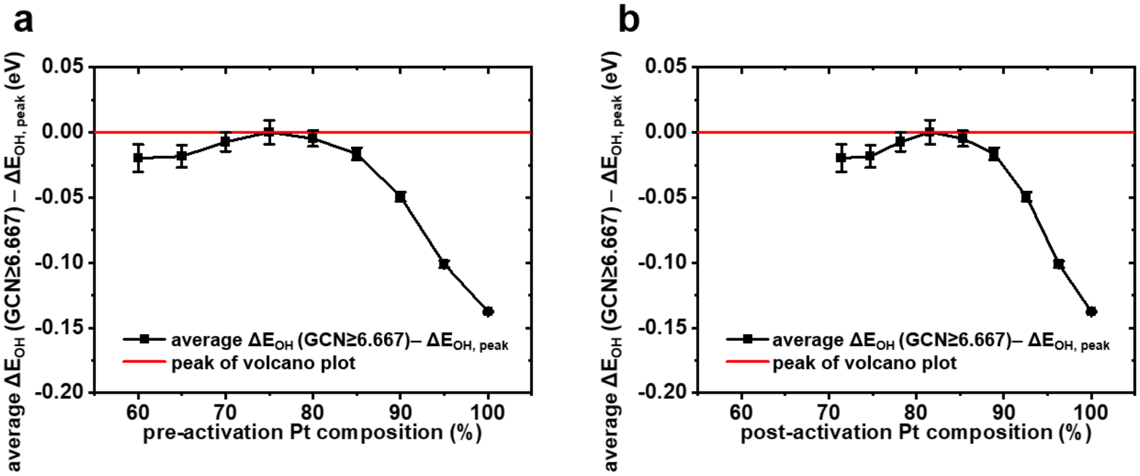

Figure S8. The predicted average *OH binding energies, referenced to that of volcano plot peak, on surface sites with coordination number equal to 9 for activated disordered octahedral nanoparticles with initial 6175 atoms as a function of Pt% (a) before KMC (pre-activation) and (b) after KMC (post-activation).

9. Catalytic activity maps as a function of post-activated Pt composition and pre-activated particle size

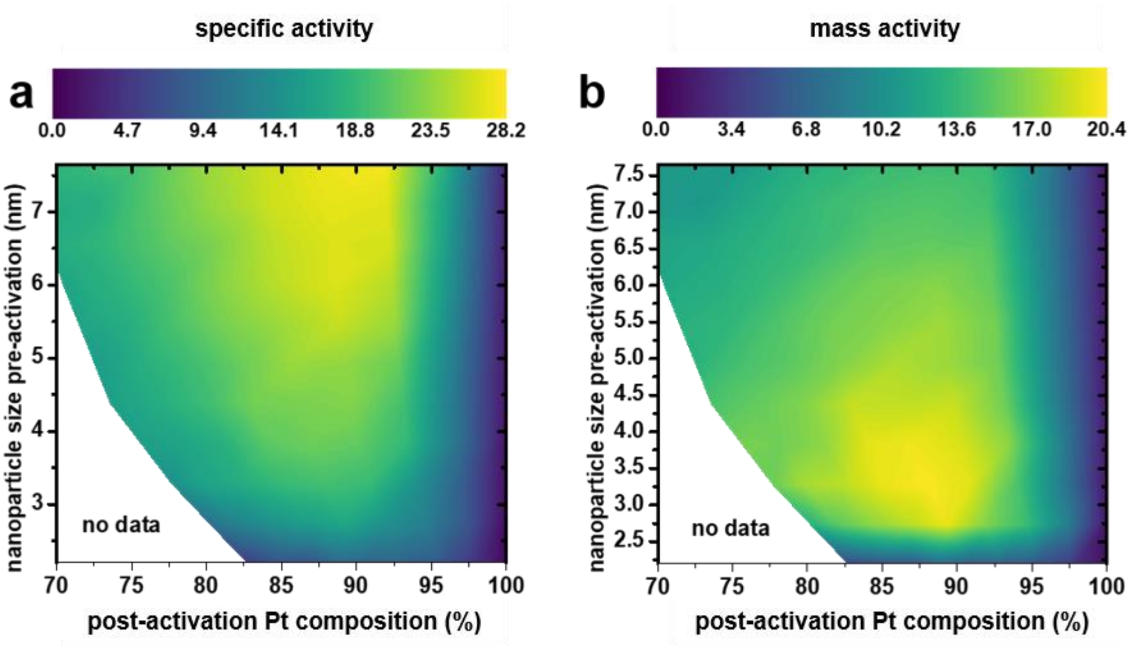

Figure S9. Predicted size-composition catalytic activity maps for the ORR. (a) Specific activity and (b) mass activity of activated disordered Pt–Ni nanoparticles. The x-axis is the Pt composition after KMC (post-activation), and the y-axis is the edge length before KMC (pre-activation). All specific and mass activity values are referenced to those of simulated commercial Pt/C.

10. Vacancy formation energies and sub-surface Pt vacancies

Table S4. On the (111) surfaces of 225-atom octahedral nanoparticles and Pt(111) as well as representative Pt-rich (111) surfaces, the DFT-calculated and CE-predicted vacancy formation energies (VFE) on the 1st and 2nd layers.

structure	position of Pt vacancy	vacancy formation energy (VFE) / eV		difference of VFE between the 2nd and 1st layers / eV	
		DFT	CE	DFT	CE
Pt_{225} particle	1st layer	0.990	0.784	-1.070	-0.206
	2nd layer	-0.080	0.579		
$Pt_{206}Ni_{19}$ particle	1st layer	1.260	0.761	-0.867	0.045
	2nd layer	0.393	0.806		
Pt(111) with 2×2 supercell	1st layer	0.895	0.660	-0.710	-0.049
	2nd layer	0.184	0.611		
Pt(111) with 4×4 supercell	1st layer	1.081	0.860	-0.653	-0.184
	2nd layer	0.428	0.676		
$Pt_{29}Ni_7$(111) with 2×2 supercell	1st layer	1.209	0.534	-0.562	0.191
	2nd layer	0.670	0.726		
$Pt_{29}Ni_7$(111) with 4×4 supercell	1st layer	1.291	0.891	-0.578	0.083
	2nd layer	0.712	0.975		

Note: Pt_{225} particle is the octahedral particle with six vertex-site Pt atoms removed (the shape is the same as the $Pt_{178}Ni_{47}$ particle in **Figure S1**; $Pt_{206}Ni_{19}$ particle is the Pt_{225} particle with Pt atoms deeper than the 2nd layer replaced by Ni atoms; $Pt_{29}Ni_7$(111) is the surface illustrated in **Figure S4**a.

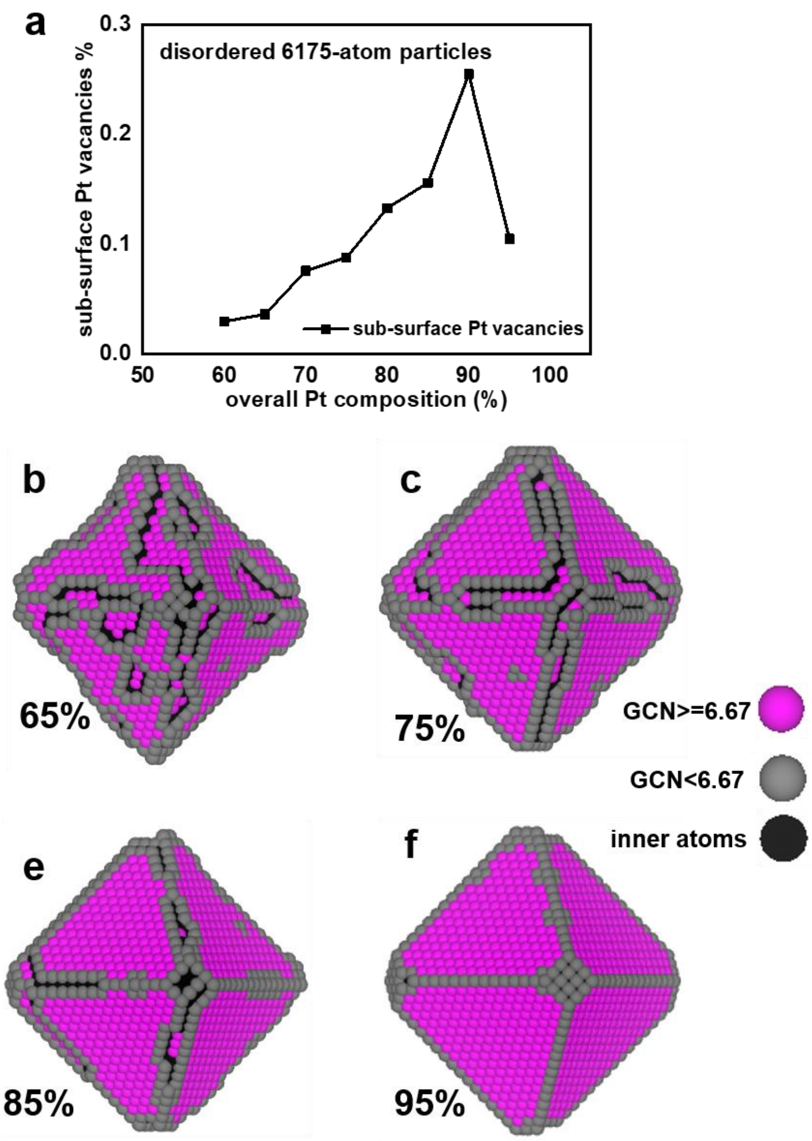

Figure S10. The (a) concentration of sub-surface Pt vacancies of activated disordered Pt–Ni particles as a function of the pre-activated Pt composition (b-e) Distribution of surface site coordination numbers of activated disordered particles with pre-activated Pt composition of (b) 65%, (c) 75%, (d) 85%, (e) 95%. In figure b-e, the surface sites on (111) surface with generalized coordination numbers (GCN) less than 6.67 have nearest-neighboring sub-surface Pt vacancies. On the fcc (111) surface, the GCN and CN of surface atoms without subsurface vacancies are 6.67 (=20 /3) and 9, respectively.

11. Determination of atomic structures of activated disordered Pt–Ni particles with Pt-rich edges

According to the experimental observation of Pt-rich edges for octahedral Pt−Ni nanoparticles from Strasser et al.'s work[28], we assume that the deposition rate of Pt atoms on edge sites is faster than that on (111) facet sites, and define the degree to which edges are more Pt-rich than (111) facets as *A* using the following equation,

$$A = \frac{\dfrac{r_{Pt}(e)}{r_{Ni}(e)}}{\dfrac{r_{Pt}(f)}{r_{Ni}(f)}} = \frac{f_{Pt,e}}{f_{Ni,e}} / \frac{r_{Pt,f}}{r_{Ni,f}}, \qquad [15]$$

where the related notations are defined as follows:

$\dfrac{r_{Pt}(e)}{r_{Ni}(e)}$ is the deposition rate of Pt referenced to that of Ni on edge sites;

$\dfrac{r_{Pt}(f)}{r_{Ni}(f)}$ is the deposition rate of Pt referenced to Ni on facet sites;

$f_{Pt,e}$ is the fraction of Pt on the edge sites;

$f_{Ni,e}$ is the fraction of Ni on the edge sites and is equivalent to $\left(1 - f_{Pt,e}\right)$;

$f_{Pt,f}$ is the fraction of Pt on the face sites;

$f_{Ni,f}$ is the fraction of Ni on the face sites and is equivalent to $\left(1 - f_{Pt,f}\right)$.

Then $f_{Ni,f}$ can be calculated using the following equation:

$$f_{Ni,f} = \frac{2Af_{Ni}}{[f_e + Af_f + (A-1)f_{Ni}] + \sqrt{[f_e + Af_f + (A-1)f_{Ni}]^2 + 4Af_{Ni}(1-A)f_f}}, \qquad [16]$$

where the related definitions are as follows:

f_e is the fraction of total atoms on the edge sites;

f_f is the fraction of total atoms on the face sites and is equivalent to $\left(1 - f_e\right)$;

f_{Ni} is the total fraction of Ni atoms within the nanoparticles;

f_{Pt} is the total fraction of Pt atoms within the nanoparticles and is equivalent to $\left(1 - f_{Ni}\right)$;

$f_{Ni,e}$ is the fraction of Ni on the edge sites and is equivalent to $\left(f_{Ni} - f_f * f_{Ni,f}\right) / f_e$.

For a 6175-atom octahedral nanoparticle, we define the width of each edge as the three-layers of atoms along the edge and immediately adjacent to the edge, which means there are 3199 atoms on edge sites and 2976 atoms on face sites ($f_e = 3199 / 6175$ and $f_f = 1 - f_e$). The $f_{Ni,f}$ and corresponding distributions of Pt and Ni atoms within the whole Pt−Ni nanoparticles with Pt-rich edges are demonstrated in **Table S5** for A=5. Accordingly the Pt and Ni atoms are randomly distributed to initialize the disordered particles, then atomic structures of activated disordered particles are simulated using the kinetic Monte Carlo simulations. The predicted average specific activities over 10 independent snapshot structures for each individual overall Pt composition are demonstrated for *A*=3, 5, 10, and $+\infty$ in **Figure S11**. We observed little change in the composition (about 85% Pt for pre-activated particles) predicted to maximize activity across all values of *A*.

Table S5. The distributions of Pt and Ni atoms between edge and face sites across the octahedral Pt-Ni nanoparticles with Pt-rich edges for *A*=5.

f_{Pt}	$f_{Ni,f}$	$f_{Ni,e}$	distributions of Pt and Ni atoms			
			$N_{Ni,e}$	$N_{Pt,e}$	$N_{Ni,f}$	$N_{Pt,f}$
0.6	0.5899	0.2234	715	2484	1755	1221
0.65	0.5290	0.1834	587	2612	1574	1402
0.7	0.4639	0.1475	472	2727	1381	1595
0.75	0.3947	0.1154	369	2830	1175	1801
0.8	0.3218	0.0867	277	2922	958	2018
0.85	0.2455	0.0611	196	3003	731	2245
0.9	0.1663	0.0384	123	3076	495	2481
0.95	0.0843	0.0180	58	3141	251	2725

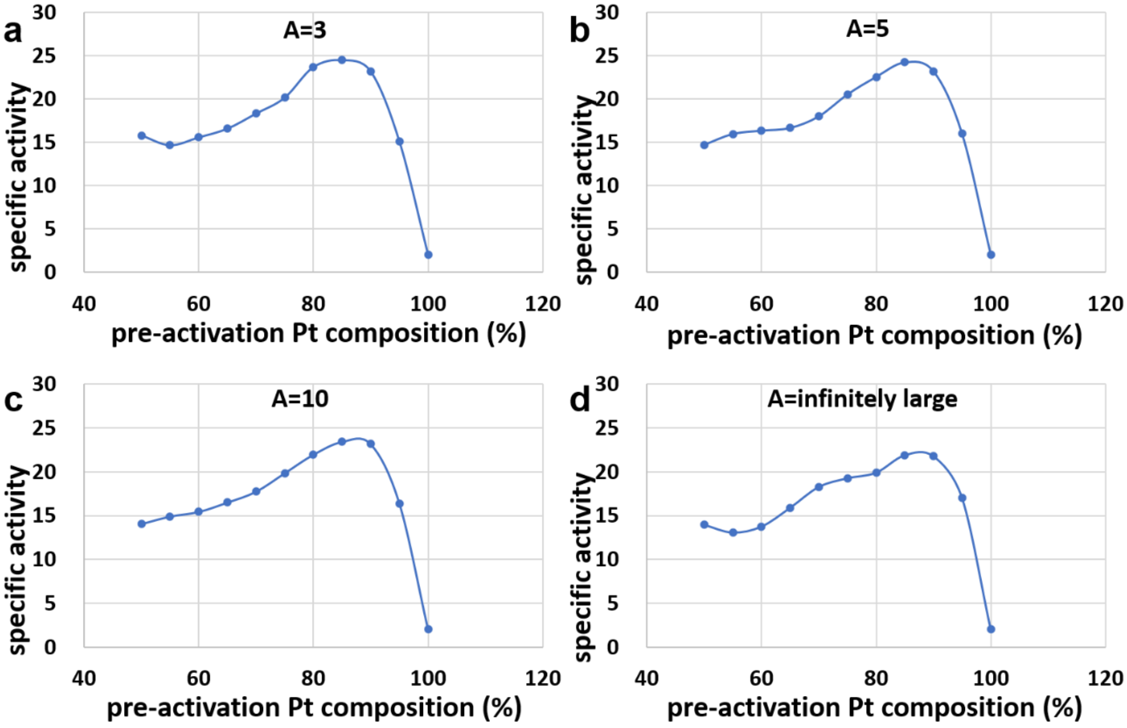

Figure S11. The average specific activities (over 10 independent snapshot structures) of activated Pt–Ni particles with Pt-rich edges as a function of pre-activation Pt composition for (a) A=3, (b) A=5, (c) A=10, and (d) A=infinitely large, respectively.

12. Predicted *OH binding energy and turnover frequency on clean particle surfaces

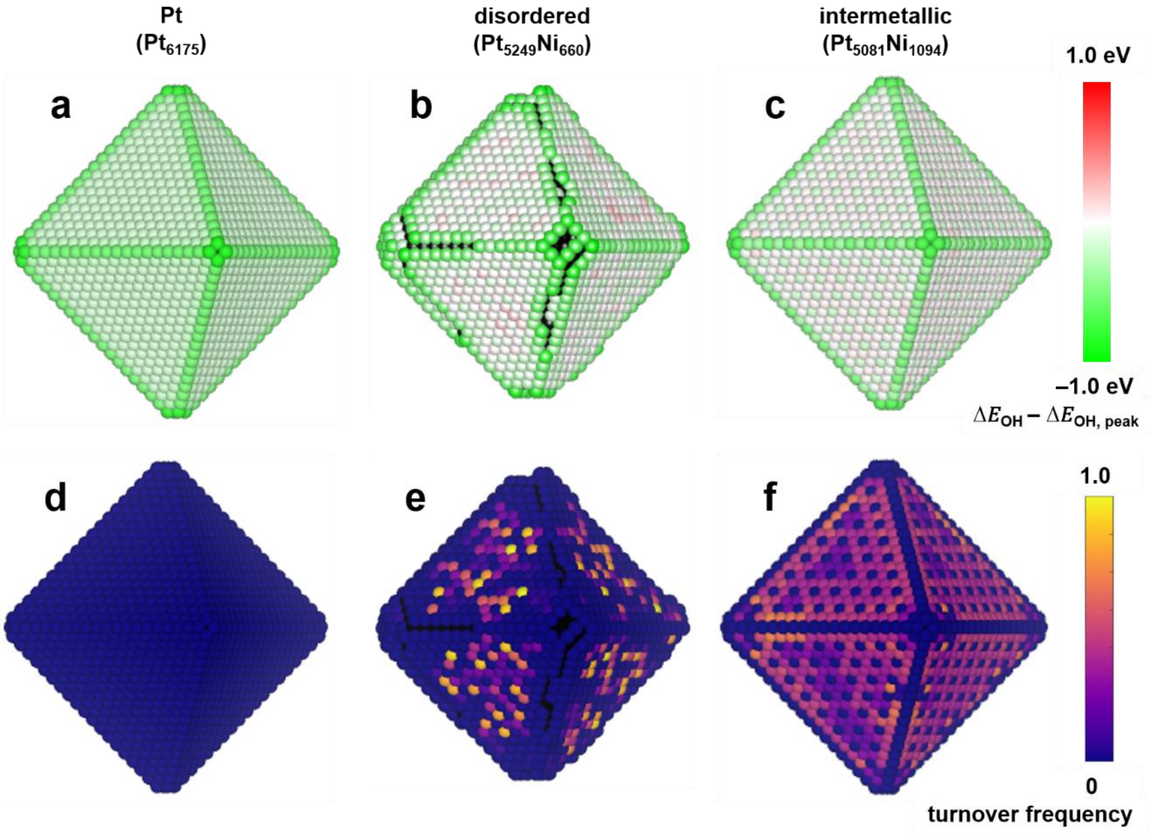

Figure S12. **Predicted *OH binding energy and turnover frequency on clean particle surfaces**. a, b, c The OH binding energy on each surface site of three representative nanoparticles with an edge length of ~5.5 nm: Pt (a), disordered $Pt_{0.85}Ni_{0.15}$ in **Figure 3**b-e (b), and intermetallic $Pt_{0.82}Ni_{0.18}$ in **Figure 3**f-i (c). d, e, f The corresponding turnover frequency (TOF) on each site. Binding energies and turnover frequencies are referenced to those at the peak of the volcano plot.

13. Layer-by-layer atomic structures of disordered $Pt_{0.85}Ni_{0.15}$ nanoparticles

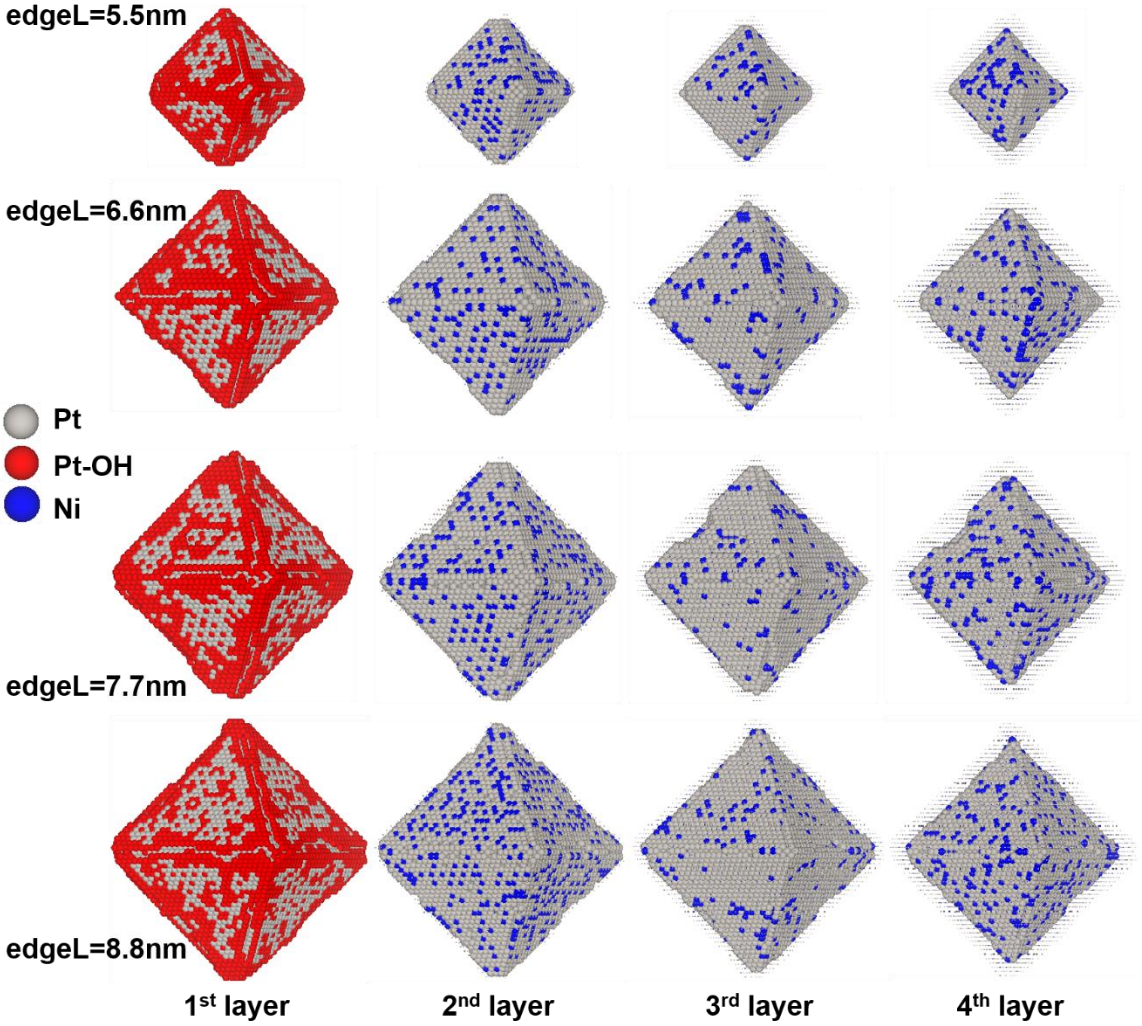

Figure S13. The layer-by-layer atomic structures of representative snapshots at 298 K for disordered $Pt_{0.85}Ni_{0.15}$ nanoparticles with adsorbed *OH determined by a KMC run on nanoparticles with edge lengths (before activation) of 5.5 nm, 6.6 nm, 7.7 nm, and 8.8 nm.

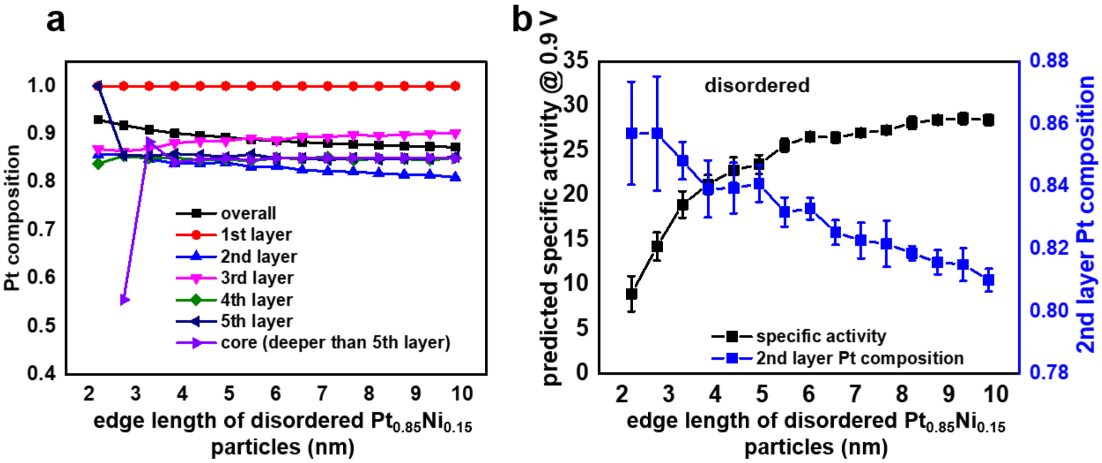

Figure S14. The (a) layer-by-layer Pt composition and (b) predicted specific activity compared with the 2nd layer Pt composition for disordered $Pt_{0.85}Ni_{0.15}$ nanoparticles as a function of particle edge length.

Table S6. The predicted layer-by-layer Pt composition for disordered $Pt_{0.85}Ni_{0.15}$ nanoparticles at 298 K as a function of edge length from 2.2 nm to 9.9 nm.

size in edge length (nm)	Pt composition (%)					
	overall	1st layer	2nd layer	3rd layer	4th layer	5th layer
2.19	93.0	100	85.7	86.9	83.9	100
2.73	91.9	100	85.7	86.4	85.4	85.6
3.28	90.9	100	84.8	86.9	85.0	85.5
3.83	90.2	100	83.9	88.1	85.1	85.9
4.37	89.7	100	84.0	88.5	84.6	85.7
4.92	89.4	100	84.1	88.6	84.7	85.2
5.47	88.9	100	83.2	89.2	84.4	85.8
6.01	88.6	100	83.3	88.7	85.0	85.0
6.56	88.3	100	82.5	89.5	84.9	85.0
7.11	88.1	100	82.3	89.4	85.3	84.6
7.66	87.9	100	82.2	89.8	84.6	85.1
8.20	87.7	100	81.9	89.7	84.9	84.7
8.75	87.5	100	81.6	89.8	84.8	84.9
9.30	87.4	100	81.5	90.1	84.6	84.9
9.84	87.3	100	81.0	90.2	85.1	85.2

14. Average *OH binding energies on (111) sites with GCN⩾6.667for disordered $Pt_{0.85}Ni_{0.15}$ nanoparticles

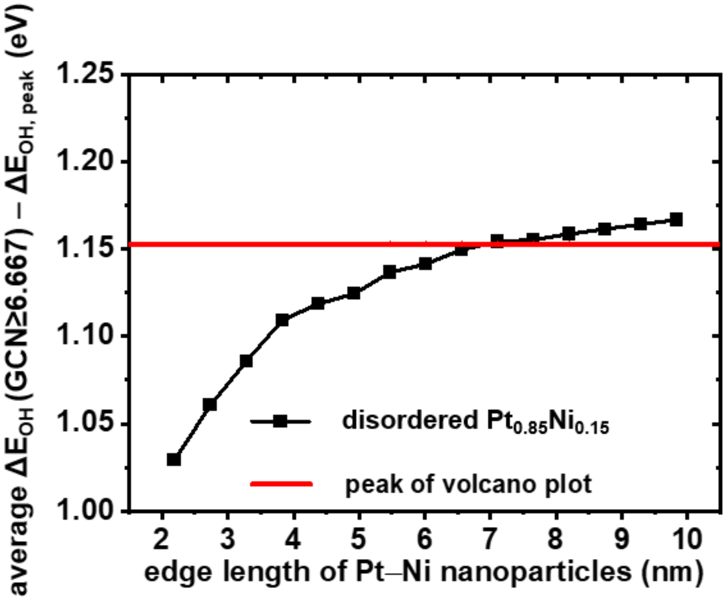

Figure S15. Average *OH binding energies on (111) sites with GCN ⩾ 6.667 for disordered $Pt_{0.85}Ni_{0.15}$ nanoparticles a function of particle size (edge length). The horizontal red line indicates the volcano plot peak.

15. Determination of chemical potentials of Pt and Ni maximizing catalytic activities of intermetallic Pt–Ni particles

To determine the atomic structures of intermetallic Pt_3Ni particles with maximal specific and mass activities, we have run Metropolis Monte Carlo[29] simulations under a grand canonical ensemble within the chemical potential window where bulk ordered Pt_3Ni is stable. To perform above simulations, firstly we refer the chemical potential difference between Pt and Ni as $\mu \equiv \mu(\mathrm{Pt}) - \mu(\mathrm{Ni})$, where reference chemical potentials of the bulk metals are set to zero. Using the same strategy in our previous work[6, 7], the window of μ where bulk Pt_3Ni is stable is between 0.04 eV and 0.50 eV according to the energies of bulk Pt, ordered Pt_3Ni and ordered Pt_2Ni_2 predicted by Pt–Ni–Vacancy cluster expansion in section 1.2. Within the μ window between 0.04 and 0.50 eV (with a grid of 0.025 eV), the thermodynamically stable atomic structures of 6175-atom nanoparticles are simulated using the Metropolis Monte Carlo simulations. The corresponding averaged specific and mass activities over 10 thermodynamic snapshot structures for each chosen value of μ are shown as a function of μ in **Figure S16**b. The maximal activities are achieved at $\mu = 0.45\ \mathrm{eV}$ and an overall Pt composition of ~82%. Thus in the present work we will choose $\mu = 0.45\ \mathrm{eV}$ when running Metropolis Monte Carlo simulations to determine the atomic structures of intermetallic Pt–Ni octahedral particles with maximal activities at varied sizes.

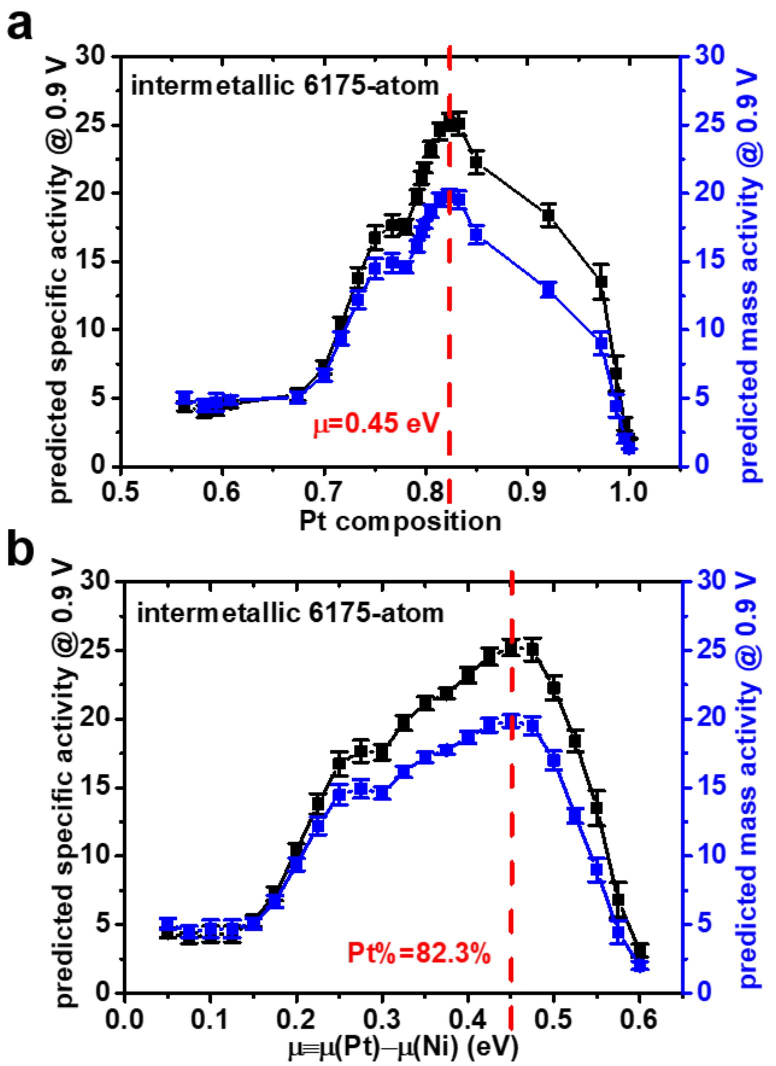

Figure S16. The predicted specific and mass activities of intermetallic octahedral nanoparticles with an edge length of 5.5 nm (6175 atoms) as a function of (a) Pt composition and (b) chemical potential difference between Pt and Ni ($\mu \equiv \mu(\mathrm{Pt}) - \mu(\mathrm{Ni})$). The chemical potential window where bulk Pt_3Ni is stable is $\mu \in [0.04, 0.5]\,\mathrm{eV}$, which was predicted based on the Pt–Ni–Vacancy cluster expansion in section 1.2.

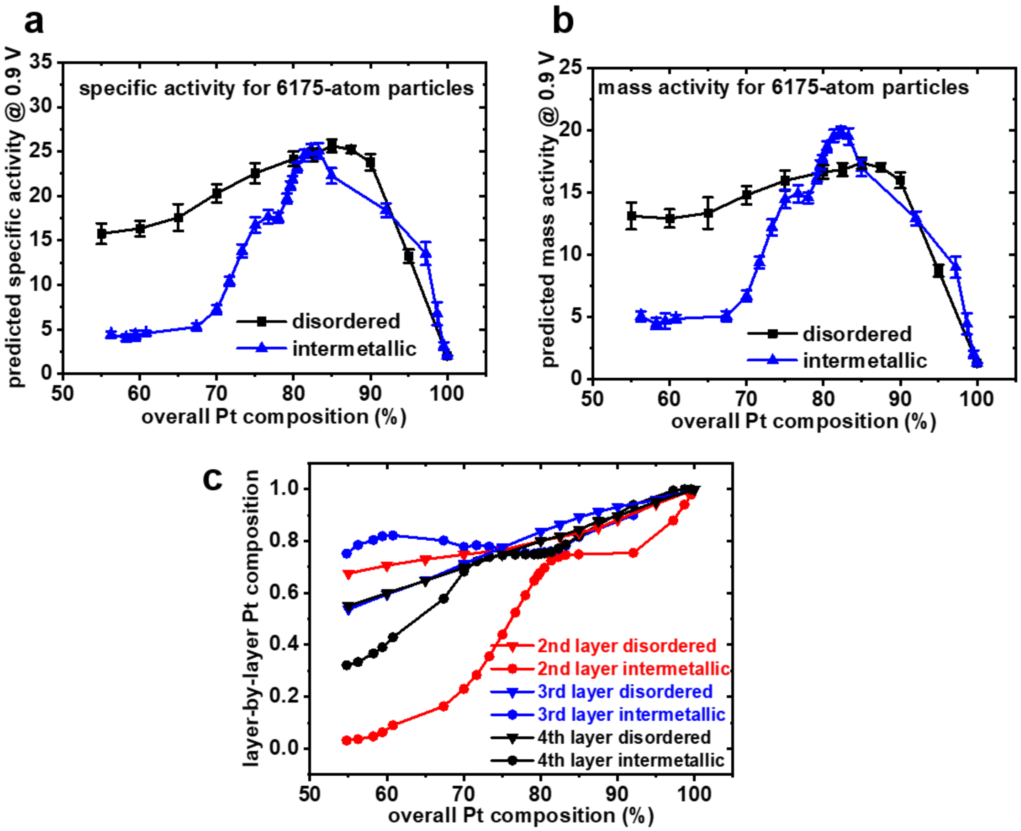

Figure S17. The predicted (a) specific activity, (b) mass activity, and (c) layer-by-layer compositions as a function of overall Pt composition for 6175-atom activated disordered and intermetallic nanoparticles. The "6175-atom" for disordered nanoparticles refers to the pre-activated number of total Pt and Ni atoms.

Table S7. Layer-by-layer Pt compositions vs. overall Pt composition for 6175-atom disordered and intermetallic nanoparticles. The 6175 atoms for disordered nanoparticles are the pre-activated number of total Pt and Ni atoms.

Pt composition (%)							
6175-atom intermetallic nanoparticles				6175-atom disordered nanoparticles			
overall	2nd layer	3rd layer	4th layer	overall	2nd layer	3rd layer	4th layer
54.76	3.17	75.15	32.14	55	67.55	53.71	54.95
56.24	3.64	78.51	33.37	60	70.60	59.49	59.92
58.22	4.71	80.42	36.67	65	72.95	64.80	64.77
59.41	6.28	81.89	39.07	70	74.83	71.19	69.76
60.79	9.00	82.18	42.90	75	76.55	77.52	74.94
67.38	16.30	80.21	57.79	80	80.06	83.59	79.98
70.00	23.01	77.76	68.26	85	83.18	89.22	84.42
71.66	28.37	78.39	72.16	90	88.11	93.25	89.65
73.31	35.50	77.87	73.88	95	94.31	95.84	95.14
75.02	43.98	76.81	74.56	100	100	100	100
76.69	52.46	75.88	74.80				
78.00	59.07	75.39	74.84				
79.16	64.73	75.16	74.84				
79.60	66.57	75.21	74.91				
79.87	67.67	75.34	74.98				
80.48	69.72	75.69	75.32				
81.36	72.49	76.03	75.74				
82.29	73.82	76.95	77.16				
83.25	74.63	78.19	78.70				
84.95	74.88	81.61	81.93				
92.05	75.48	90.05	93.92				
97.23	87.90	99.40	99.50				

16. Layer-by-layer atomic structures of intermetallic Pt–Ni nanoparticles

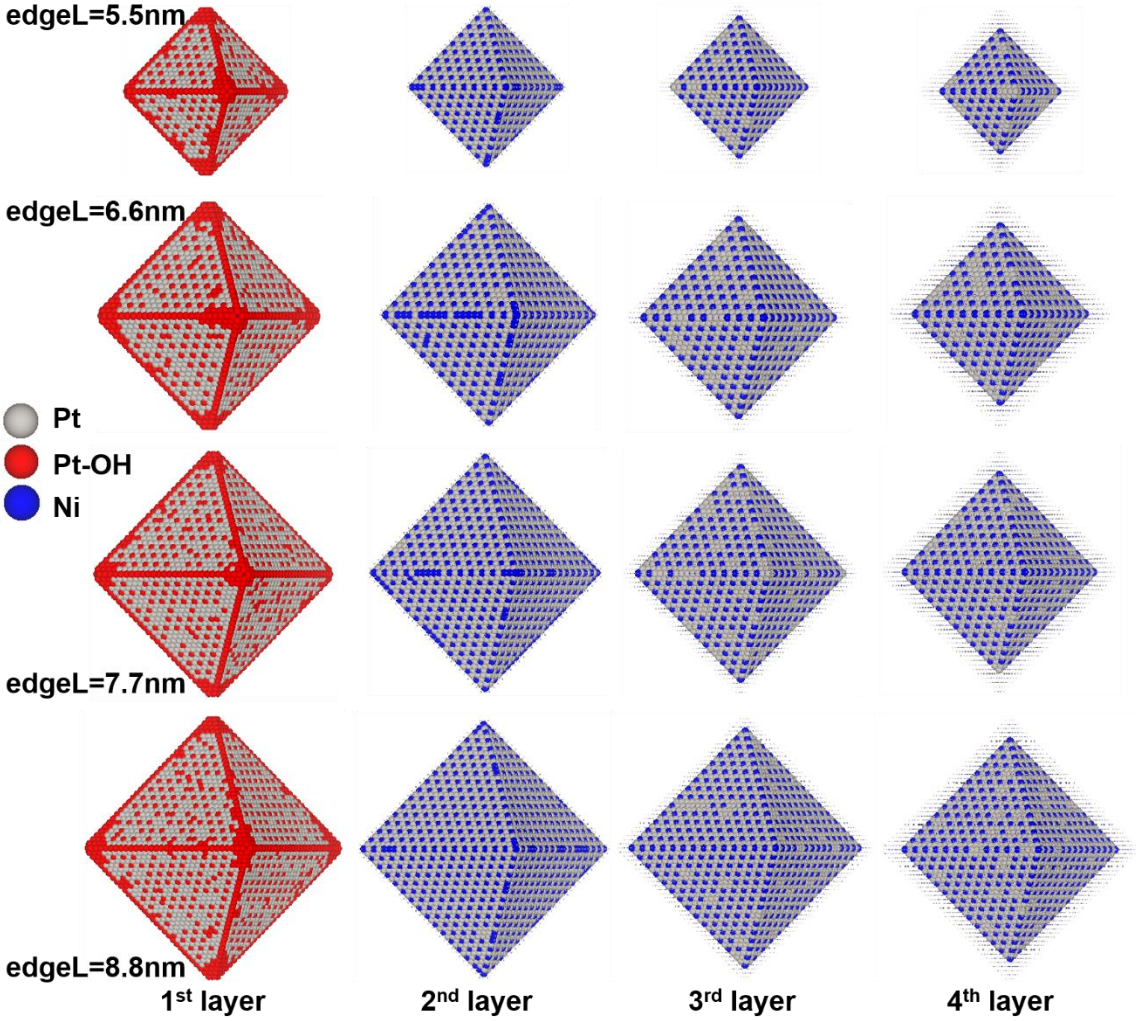

Figure S18. The layer-by-layer atomic structures of representative snapshots at 298 K for intermetallic Pt–Ni nanoparticles at μ=0.45 eV with adsorbed *OH determined by KMC run at an edge length of 5.5 nm, 6.6 nm, 7.7 nm, and 8.8 nm. There exists an $L1_2$ structure on subsurface layers.

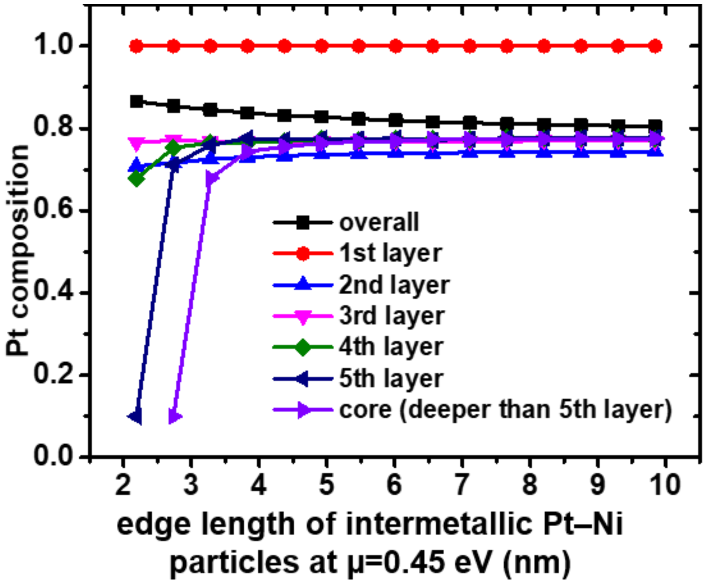

Figure S19. The layer-by-layer Pt composition for intermetallic Pt–Ni nanoparticles at μ=0.45 eV as a function of particle edge length.

Table S8. The predicted layer-by-layer Pt composition for intermetallic Pt–Ni nanoparticles at μ=0.45 eV at 298 K as a function of edge length from 2.2 nm to 9.9 nm.

size in edge length (nm)	Pt composition (%)					
	overall	1st layer	2nd layer	3rd layer	4th layer	5th layer
2.19	86.6	100	70.8	76.5	67.8	10
2.73	85.4	100	71.6	77.1	75.3	71.1
3.28	84.5	100	72.6	76.8	76.5	75.9
3.83	83.8	100	73.0	76.8	76.6	77.6
4.37	83.1	100	73.4	76.6	76.9	77.2
4.92	82.8	100	73.7	76.9	77.4	77.5
5.47	82.3	100	73.8	76.9	77.2	77.4
6.01	82.0	100	74.1	77.0	77.4	77.6
6.56	81.6	100	73.9	76.7	77.4	77.1
7.11	81.4	100	74.2	76.8	77.3	77.4
7.66	81.1	100	74.2	76.8	77.6	77.6
8.20	81.0	100	74.2	77.0	77.6	77.6
8.75	80.8	100	74.2	77.0	77.6	77.8
9.30	80.6	100	74.3	77.1	77.6	77.6
9.84	80.5	100	74.4	77.0	77.5	77.7

17. Mass activity of disordered and intermetallic nanoparticles as a function of size

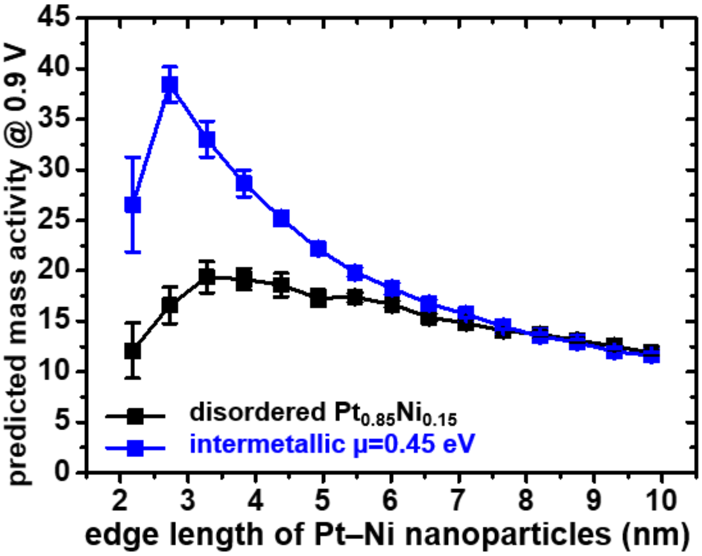

Figure S20. Predicted mass activity of disordered $Pt_{0.85}Ni_{0.15}$ nanoparticles and intermetallic Pt–Ni nanoparticles at μ=0.45 eV at 298K as a function of edge length. The mass activity values are referenced to that of simulated commercial Pt/C. The corresponding predicted specific activities are provided in **Figure 2**c.

18. Average *OH binding energies on (111) sites with GCN⩾6.667 for disordered $Pt_{0.85}Ni_{0.15}$ and intermetallic Pt–Ni nanoparticles

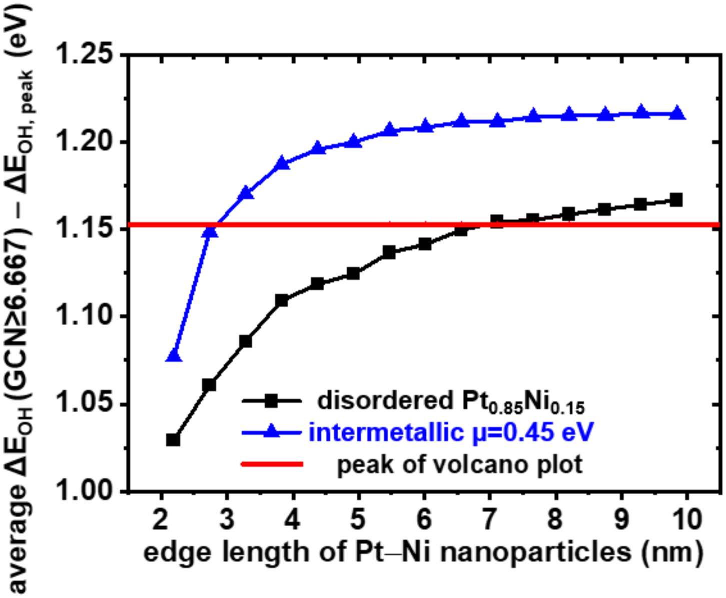

Figure S21. Average *OH binding energies on (111) sites with GCN⩾6.667 for disordered $Pt_{0.85}Ni_{0.15}$ nanoparticles and intermetallic Pt–Ni nanoparticles at μ=0.45 eV as a function of particle size (edge length). The horizontal red line indicates the volcano plot peak.

19. Predicted ORR activities of activated disordered particles with varied shapes

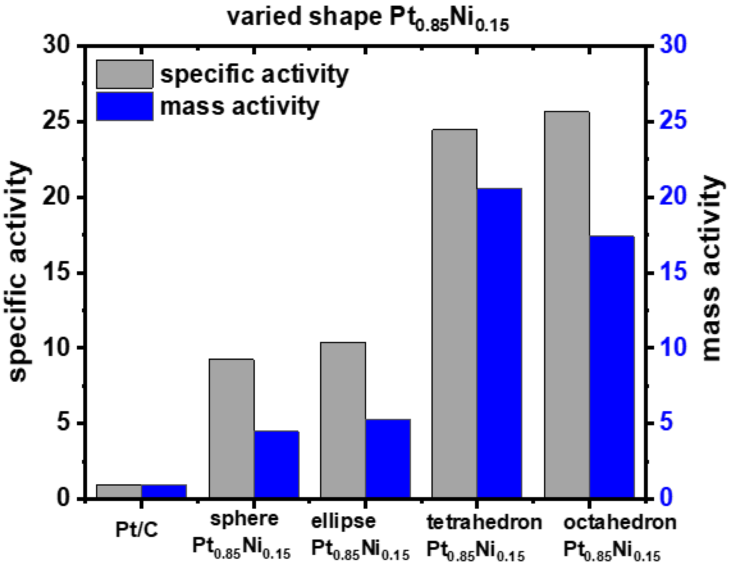

Figure S22. The predicted specific and mass activities of 6000-atom activated disordered $Pt_{0.85}Ni_{0.15}$ particles with octahedral, tetrahedral, spherical and ellipsoidal shapes. Before predicting activities, the Pt – Ni particles have been activated (simulated by KMC). The predicted values are referenced to those of commercial Pt/C.

20. Distribution of OH binding energy and turnover frequencies

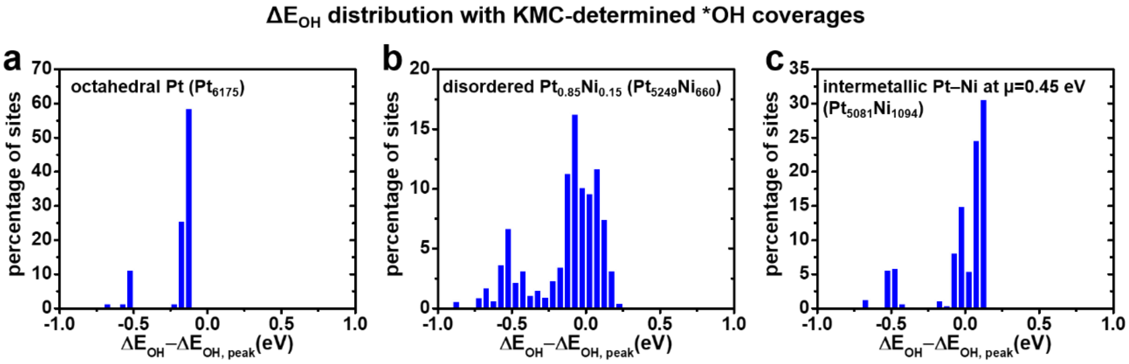

Figure S23. Under the KMC-determined *OH coverages, the histograms showing the distribution of average ΔE_{OH} on the surface of three representative nanoparticles in **Figure 4**a-c: (a) Pt, (b) disordered $Pt_{0.85}Ni_{0.15}$ nanoparticles, and (c) intermetallic Pt–Ni nanoparticles at μ=0.45 eV, respectively. The range of distribution of ΔE_{OH} in figures (a-c) is [–1.0, 1.0] eV, and the width of histograms is 0.05 eV. For each KMC simulation, the numbers of both equilibration steps and recording steps are 15 times the number of adsorption sites. The average values of ΔE_{OH} were averaged over the recording steps.

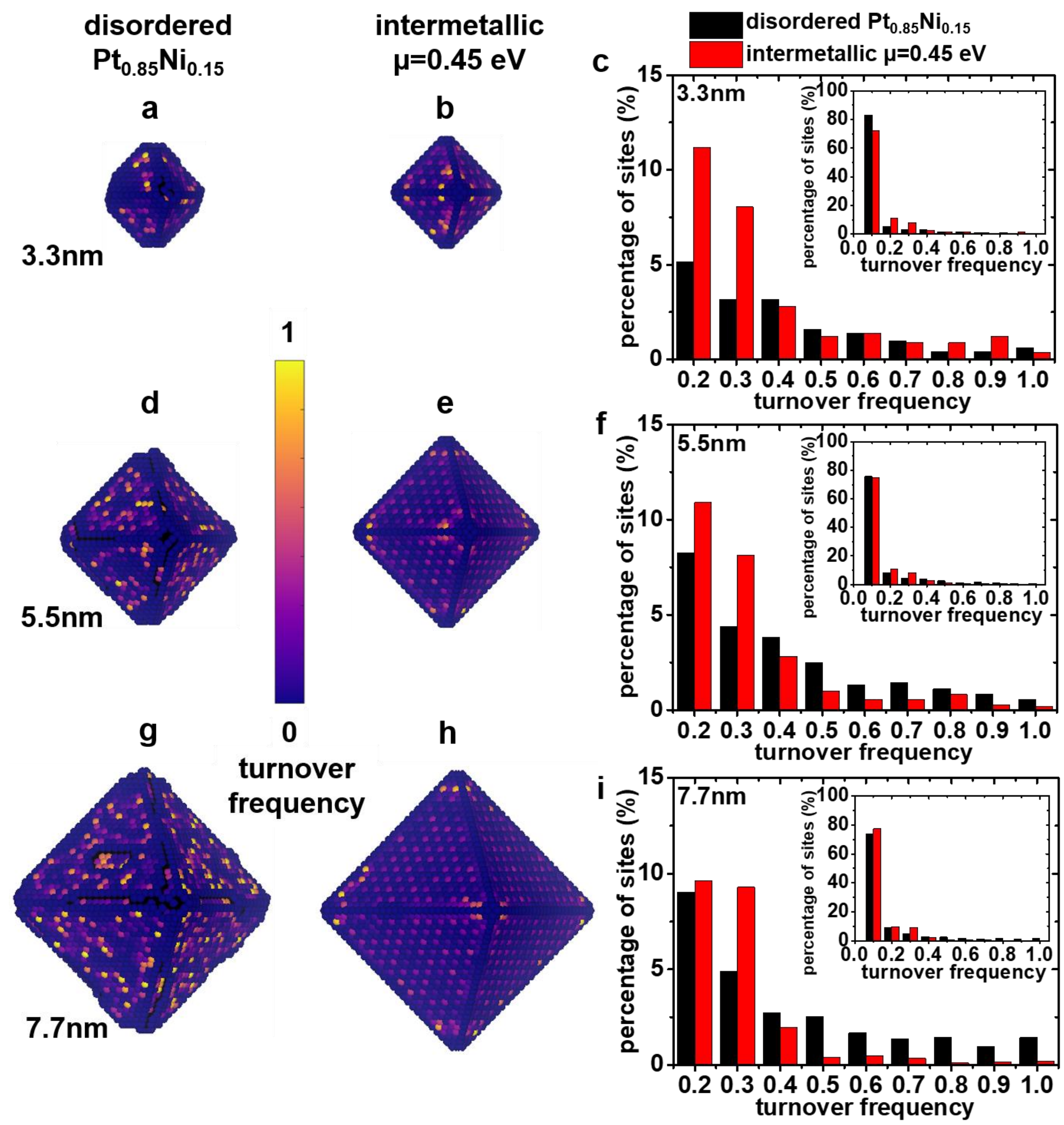

Figure S24. Under the KMC-determined *OH coverages, the site-specific average turnover frequency for each surface site of (a, d, g) disordered $Pt_{0.85}Ni_{0.15}$ nanoparticles and (b, e, h) intermetallic Pt–Ni nanoparticles at μ=0.45 eV in an edge length of (a, b) 3.3 nm, (d, e) 5.5 nm, and (g, h) 7.7 nm, respectively. (c, f, i) The corresponding histograms of average turnover frequencies. Both the kinetic Monte Carlo simulations to determine the disordered particles and Metropolis Monte Carlo simulations to determine intermetallic particles were run at 298K. Figures d and e are the same as **Figure 4**e, f. The histograms were constructed using all surface sites.

Reference

(1) Ising, E. Beitrag zur Theorie des Ferromagnetismus. *Zeitschrift für Physik* **1925,** 31, 253-258.

(2) Sanchez, J. M. Cluster Expansion and the Configurational Theory of Alloys. *Phys. Rev. B* **2010,** 81, 224202.

(3) Sanchez, J. M.; Ducastelle, F.; Gratias, D. Generalized Cluster Description of Multicomponent Systems. *Phys. A (Amsterdam, Neth.)* **1984,** 128, 334-350.

(4) Van de Walle, A.; Ceder, G. Automating First-Principles Phase Diagram Calculations. *J. Phase Equilib.* **2002,** 23, 348-359.

(5) Mueller, T.; Ceder, G. *Ab initio* Study of the Low-Temperature Phases of Lithium Imide. *Phys. Rev. B* **2010,** 82, 174307.

(6) Cao, L.; Mueller, T. Rational Design of Pt_3Ni Surface Structures for the Oxygen Reduction Reaction. *J. Phys. Chem. C* **2015,** 119, 17735-17747.

(7) Cao, L.; Niu, L.; Mueller, T. Computationally generated maps of surface structures and catalytic activities for alloy phase diagrams. *Proc. Natl. Acad. Sci. U. S. A.* **2019,** 116, 22044-22051.

(8) Cao, L.; Zhao, Z.; Liu, Z.; Gao, W.; Dai, S.; Gha, J., et al. Differential Surface Elemental Distribution Leads to Significantly Enhanced Stability of PtNi-Based ORR Catalysts. *Matter* **2019,** 1, 1567-1580.

(9) Li, C.; Raciti, D.; Pu, T.; Cao, L.; He, C.; Wang, C., et al. Improved Prediction of Nanoalloy Structures by the Explicit Inclusion of Adsorbates in Cluster Expansions. *J. Phys. Chem. C* **2018,** 122, 18040-18047.

(10) Huang, X.; Zhao, Z.; Cao, L.; Chen, Y.; Zhu, E.; Lin, Z., et al. High-performance transition metal–doped Pt3Ni octahedra for oxygen reduction reaction. *Science* **2015,** 348, 1230-1234.

(11) Cao, L.; Mueller, T. Theoretical Insights into the Effects of Oxidation and Mo-Doping on the Structure and Stability of Pt-Ni Nanoparticles *Nano Lett.* **2016,** 16, 7748-7754.

(12) Jia, Q.; Zhao, Z.; Cao, L.; Li, J.; Ghoshal, S.; Davies, V., et al. Roles of Mo Surface Dopants in Enhancing the ORR Performance of Octahedral PtNi Nanoparticles. *Nano Lett.* **2018,** 18, 798-804.

(13) Mueller, T.; Ceder, G. Exact Expressions for Structure Selection in Cluster Expansions. *Phys. Rev. B* **2010,** 82, 184107.

(14) Norskov, J. K.; Rossmeisl, J.; Logadottir, A.; Lindqvist, L.; Kitchin, J. R.; Bligaard, T., et al. Origin of the Overpotential for Oxygen Reduction at a Fuel-Cell Cathode. *J. Phys. Chem. B* **2004,** 108, 17886-17892.

(15) Mueller, T.; Ceder, G. Bayesian Approach to Cluster Expansions. *Phys. Rev. B* **2009,** 80, 024103.

(16) Calle-Vallejo, F.; Martínez, J. I.; García-Lastra, J. M.; Sautet, P.; Loffreda, D. Fast Prediction of Adsorption Properties for Platinum Nanocatalysts with Generalized Coordination Numbers. *Angew. Chem., Int. Ed.* **2014,** 53, 8316-8319.

(17) Calle-Vallejo, F.; Tymoczko, J.; Colic, V.; Vu, Q. H.; Pohl, M. D.; Morgenstern, K., et al. Finding optimal surface sites on heterogeneous catalysts by counting nearest neighbors. *Science* **2015,** 350, 185.

(18) Karlberg, G. S.; Rossmeisl, J.; Norskov, J. K. Estimations of Electric Field Effects on the Oxygen Reduction Reaction based on the Density Functional Theory. *Phys. Chem. Chem. Phys.* **2007,** 9, 5158-5161.

(19) Rossmeisl, J.; Logadottir, A.; Norskov, J. K. Electrolysis of Water on (Oxidized) Metal Surfaces. *Chem. Phys.* **2005,** 319, 178-184.

(20) Rossmeisl, J.; Karlberg, G. S.; Jaramillo, T.; Norskov, J. K. Steady State Oxygen Reduction and Cyclic Voltammetry. *Faraday Discuss.* **2008,** 140, 337-346.

(21) Viswanathan, V.; Hansen, H. A.; Rossmeisl, J.; Nørskov, J. K. Unifying the 2e– and 4e– Reduction of Oxygen on Metal Surfaces. *J. Phys. Chem. Lett.* **2012,** 3, 2948-2951.

(22) Viswanathan, V.; Hansen, H. A.; Rossmeisl, J.; Nørskov, J. K. Universality in Oxygen Reduction Electrocatalysis on Metal Surfaces. *ACS Catal.* **2012,** 2, 1654-1660.

(23) Schulze, T. P. Efficient kinetic Monte Carlo simulation. *J. Comput. Phys.* **2008,** 227, 2455-2462.

(24) Serebrinsky, S. A. Physical Time Scale in Kinetic Monte Carlo Simulations of Continuous-Time Markov Chains. *Phys. Rev. E* **2011,** 83, 037701.

(25) Gasteiger, H. A.; Kocha, S. S.; Sompalli, B.; Wagner, F. T. Activity Benchmarks and Requirements for Pt, Pt-Alloy, and non-Pt Oxygen Reduction Catalysts for PEMFCs. *Appl. Catal., B* **2005,** 56, 9-35.

(26) Paulus, U. A.; Wokaun, A.; Scherer, G. G.; Schmidt, T. J.; Stamenkovic, V.; Radmilovic, V., et al. Oxygen Reduction on Carbon-Supported Pt−Ni and Pt−Co Alloy Catalysts. *J. Phys. Chem. B* **2002,** 106, 4181-4191.

(27) Stamenkovic, V. R.; Fowler, B.; Mun, B. S.; Wang, G.; Ross, P. N.; Lucas, C. A., et al. Improved Oxygen Reduction Activity on $Pt_3Ni(111)$ via Increased Surface Site Availability. *Science* **2007,** 315, 493-497.

(28) Gan, L.; Cui, C.; Heggen, M.; Dionigi, F.; Rudi, S.; Strasser, P. Element-Specific Anisotropic Growth of Shaped Platinum Alloy Nanocrystals. *Science* **2014,** 346, 1502-1506.

(29) Metropolis, N.; Rosenbluth, A. W.; Rosenbluth, M. N.; Teller, A. H.; Teller, E. Equation of State Calculations by Fast Computing Machines. *J. Chem. Phys.* **1953,** 21, 1087-1092.